Clim Dyn (2014) 43:2349–2375
DOI 10.1007/s00382-014-2058-z

The atmospheric component of the Mediterranean Sea water budget in a WRF multi-physics ensemble and observations

Alejandro Di Luca · Emmanouil Flaounas · Philippe Drobinski · Cindy Lebeaupin Brossier

Received: 9 July 2013 / Accepted: 16 January 2014 / Published online: 2 February 2014

Abstract The use of high resolution atmosphere–ocean coupled regional climate models to study possible future climate changes in the Mediterranean Sea requires an accurate simulation of the atmospheric component of the water budget (i.e., evaporation, precipitation and runoff). A specific configuration of the version 3.1 of the weather research and forecasting (WRF) regional climate model was shown to systematically overestimate the Mediterranean Sea water budget mainly due to an excess of evaporation ($\sim$1,450 mm yr^{-1}) compared with observed estimations ($\sim$1,150 mm yr^{-1}). In this article, a 70-member multi-physics ensemble is used to try to understand the relative importance of various sub-grid scale processes in the Mediterranean Sea water budget and to evaluate its representation by comparing simulated results with observed-based estimates. The physics ensemble was constructed by performing 70 1-year long simulations using version 3.3 of the WRF model by combining six cumulus, four surface/planetary boundary layer and three radiation schemes. Results show that evaporation variability across the multi-physics ensemble ($\sim$10 % of the mean evaporation) is dominated by the choice of the surface layer scheme that explains more than $\sim$70 % of the total variance and that the overestimation of evaporation in WRF simulations is generally related with an overestimation of surface exchange coefficients due to too large values of the surface roughness parameter and/or the simulation of too unstable surface conditions. Although the influence of radiation schemes on evaporation variability is small ($\sim$13 % of the total variance), radiation schemes strongly influence exchange coefficients and vertical humidity gradients near the surface due to modifications of temperature lapse rates. The precipitation variability across the physics ensemble ($\sim$35 % of the mean precipitation) is dominated by the choice of both cumulus ($\sim$55 % of the total variance) and planetary boundary layer ($\sim$32 % of the total variance) schemes with a strong regional dependence. Most members of the ensemble underestimate total precipitation amounts with biases as large as 250 mm yr^{-1} over the whole Mediterranean Sea compared with ERA Interim reanalysis mainly due to an underestimation of the number of wet days. The larger number of dry days in simulations is associated with a deficit in the activation of cumulus schemes. Both radiation and planetary boundary layer schemes influence precipitation through modifications on the available water vapor in the boundary layer generally tied with changes in evaporation.

Keywords Regional climate model · Evaporation · Precipitation · Parameterizations · Cumulus · Planetary boundary layer

Abbreviations

ACM2	Version 2 of the asymmetrical convective model scheme
BMJ	Betts–Miller–Janjic scheme
CTL	Control
CU	Cumulus scheme
ERAI	ERA Interim reanalysis

A. Di Luca (✉) · E. Flaounas · P. Drobinski
Laboratoire de Météorologie Dynamique, Institute Pierre Simon Laplace, CNRS and École Polytechnique,
91128 Palaiseau Cedex, France
e-mail: alejandrodiluca@gmail.com

A. Di Luca
Climate Change Research Centre, University of New South Wales, Sydney, NSW 2052, Australia

C. L. Brossier
CNRM-GAME, UMR3589, Météo-France and CNRS,
42, Avenue G.-Coriolis, 31057 Toulouse, France

G3D	Grell 3D ensemble scheme
HyMeX	Hydrological cycle in the Mediterranean experiment
KF	Kain–Fritsch scheme
MED-CORDEX	Mediterranean contribution to the Coordinated Regional climate Downscaling Experiment
MM5	Fifth-generation of the Mesoscale Model
MPE	Multi-physics ensemble
MSWB	Mediterranean Sea water budget
MT	Modified Tiedtke scheme
MYJ	Mellor–Yamada–Janjic scheme
MYNN	Mellor–Yamada–Nakanishi–Niino scheme
NEMO	Nucleus for European modelling of the ocean
NSAS	New Simplified Arakawa–Schubert
PBL	Planetary boundary layer scheme
RAD	Radiation scheme
RCM	Regional climate model
RRTM	Rapid radiative transfer Model scheme
RRTMG	Rapid radiative transfer model for application to GCMs scheme
SAS	Simplified Arakawa–Schubert scheme
SL	Surface layer scheme
SPBL	Surface and planetary boundary layer scheme
SST	Sea surface temperature
WRF	Weather research and forecasting
YSU	Yonsey University scheme

1 Introduction

The climate of the Mediterranean Sea basin results from a complicated interaction between the large-scale atmospheric circulation (e.g., position and intensity of the storm tracks and the subtropical high pressure belt) and fine-scale surface forcings. One such an important surface forcing is the orography. The complex orography surrounding the Mediterranean Sea interacts with synoptic scale meteorological systems inducing important modifications in regional circulations like Mistral and Tramontane wind systems in southern France (Guenard et al. 2005), cyclogenesis in the Gulf of Genoa (Trigo et al. 2002) and significant changes in the local climate (Peixoto et al. 1982). Another important fine-scale surface forcing is given by the presence of land–sea contrasts and sea surface temperature (SST) gradients. In winter, land–sea contrasts strongly increases low-level baroclinicity favoring cyclogenesis in several regions along the Mediterranean (e.g., Aegean and Black Seas) with an important influence on the climatology of the hydrological cycle (Trigo et al. 2002).

Table 1 Long-term mean estimations of the Mediterranean Sea averaged evaporation (fourth column; in mm yr^{-1}), precipitation (fifth column; in mm yr^{-1}) and water budget (sixth column; in mm yr^{-1}) from a variety of observed and simulated datasets (first column)

	Δx	Period	E	P	E–P
HOAPS3		89-05	1,150	260	883
HOAPS3—GPCP		89-05/89-08	1,150	526	609
OAFlux—GPCP		89-08	1,133	526	607
NOC—CMAP (Sanchez-Gomez et al. 2011)		80-04/89-08	1,115	467	648
UWM/COADS—CMAP (Mariotti et al. 2002)		79-93	1,176	477	699
ERA-40		80-99	1,055	363	692
ERAI		89-08	1,140	410	730
WRF3.1-CTL	50	89-08	1,443	326	1,116
WRF3.1-CTL (Drobinski et al. 2012)	20	89-08	1,533	499	1,034
WRF3.1-CTL-NEMO (Drobinski et al. 2012)	20	89-08	1,442	482	980
ENS-RCM (Sanchez-Gomez et al. 2011)	25	61-00	1,254	442	812

The first column also includes a bibliographic source when needed. The second column presents the horizontal grid spacing (Δx; in km) of simulated data and the third column shows the the averaging time period for the various datasets. All WRF3.1 simulations were performed using the CTL physics package, namely, RRTMG for the atmospheric radiation scheme, YSU for the surface/planetary boundary layer scheme and KF for the cumulus scheme. Note that the HOAPS3 satellite product is only available over the open ocean

The need of a more detailed description of the topography and its influence on the atmospheric flow was a primary motivation for the development of the nesting regional climate modelling (RCM) technique (Giorgi et al. 2001; Laprise 2008). More recently, the effects of fine-scale variations in land–sea contrasts and in SST gradients have been explicitly considered within the RCM technique by coupling the atmospheric RCM with a limited-area ocean model, leading to the development of atmosphere–ocean RCMs (Somot et al. 2008; Artale et al. 2009; Drobinski et al. 2012). The use of atmosphere–ocean RCMs can be crucial in the context of a Mediterranean climate becoming warmer and drier (Christensen et al. 2007; Mariotti et al. 2008; Dubois et al. 2011) due to the possible modifications in the Mediterranean circulation. In particular, the Mediterranean Sea water budget (MSWB) constitutes a key component of the coupled system because it is the primary triggering of the thermohaline circulation (Béranger et al. 2010).

Following Mariotti et al. (2002), the spatially averaged MSWB can be described using the following equation:

$$\frac{\partial W}{\partial t} = P + R - E + A + B, \quad (1)$$

where W is the total volume of water in the Mediterranean Sea, P the total water falling as precipitation, E the total evaporation, R the river runoff in the basin and A and B the water flow from/to the Atlantic ocean and the Black sea respectively. Table 1 shows long-term mean values of the atmospheric water balance components E, P and $E - P$ averaged over the whole Mediterranean Sea from a variety of sources (Mariotti et al. 2002; Sanchez-Gomez et al. 2011; Drobinski et al. 2012). Every dataset shows an excess of evaporation over precipitation that leads to a net loss of fresh water that varies between about 600 and 730 mm yr^{-1} for reanalyses and satellite products. Over relatively long periods (e.g., a few years), the deficit of fresh water and the associated salinification of the surface layer are partly balanced by the runoff contribution [$R \approx 150$ mm yr^{-1} according to Dubois et al. (2011)] but specially through the inflow of relatively fresh water from the Atlantic Ocean via the Strait of Gibraltar [$A \approx 470-1{,}100$ mm yr^{-1} according to Dubois et al. (2011)].

The representation of the atmospheric component of the MSWB (evaporation, precipitation and runoff) by high-resolution RCMs have been recently studied in a number of articles. Sanchez-Gomez et al. (2011) used various observational datasets and 12 RCMs driven at their boundaries by ERA-40 reanalysis to estimate the fresh water budget over the Mediterranean Sea (see Table 1). They found that the water budget as simulated using RCMs is generally within the observational uncertainty although the observational uncertainty can be quite large. They also show that RCMs tend to overestimate the mean evaporation over the Mediterranean Sea compared to observations, showing that good performances in the simulation of the water budget can arise from the compensation of evaporation and precipitation errors. On the other hand, based on observations of the water flow through the Strait of Gibraltar, they suggest that the observed evaporation may be underestimated over the Mediterranean. Dubois et al. (2011) used a four-member ensemble of atmosphere–ocean RCMs to study the MSWB in present and future climates. Averaged over the Mediterranean, atmosphere–ocean RCMs water budget estimations are similar to those found for only-atmospheric RCMs in Sanchez-Gomez et al. (2011) although the spread between the atmosphere–ocean RCMs is larger compared to atmospheric RCMs mainly due to changes in air–sea fluxes (i.e., evaporation) induced by differences in the SST fields.

Drobinski et al. (2012) have shown that the particular configuration of the version 3.1 of the weather research and forecasting (WRF) model described in Lebeaupin Brossier et al. (2011) tends to systematically overestimate evaporation by nearly 300 mm yr^{-1} (about 20 % of the total evaporation) leading to an overestimation of the water balance in the Mediterranean Sea region of about 300 mm yr^{-1} ($\approx 30\,\%$ in relative terms) compared with observed-based estimations. This overestimation appears for a variety of simulations performed with the version 3.1 of WRF (WRF3.1): forced by observed SSTs, coupled with the Nucleus for European Modelling of the Ocean (NEMO) model and run with horizontal grid spacings of 20 or 50 km. When considering the WRF3.1-NEMO coupled simulation, the overestimation of the fresh water loss can induce an extra salinification and cooling of sea surface waters. This anomalous densification of the surface layer in the NEMO ocean model cannot be fully compensated by exchanges with the Atlantic Ocean because this term is relaxed toward an observed climatology. As a consequence, an anomaly in the intensity/frequency of deep water formations develops in the NEMO ocean model. Figure 1 shows a drift in the content of salt of the whole Mediterranean Sea (left panel) and of the layer under 600 m-depth (right panel) in the NEMO simulation coupled with WRF3.1 for the period 1989–2008. Figure 1 also includes estimations of salt contents from Rixen (2005) and from Ingleby and Huddleston (2007). In the WRF3.1-NEMO simulation, the rate of increase in salinity is of 3.3×10^{-3} and 1.7×10^{-3} psu/yr in the whole Mediterranean Sea and in the deep layer respectively. In both cases, salinity drifts in the coupled experiment are too large compared to observed trends during the same period.

Several authors (Herrmann and Somot 2008; Artale et al. 2009; Béranger et al. 2010) have shown the preponderant role of the atmospheric boundary conditions in oceanic simulations over the Mediterranean by quantifying the impact of the source and horizontal resolution of the data used to drive the ocean model. Air–sea fluxes in RCM simulations depend on a variety of factors including but not limited to the quality and resolution of the surface boundary conditions and the general configuration of the RCM such as its resolution, domain size and the physical parameterizations used to represent subgrid scale processes. In this article, a multi-physics ensemble (MPE) is generated using the WRF model forced by ERA Interim reanalysis boundary conditions to try to quantify and understand differences in the simulation of the atmospheric component of the MSWB. Particular emphasis is given to the evaporation field due to its higher relative importance in the total MSWB and the large biases found in its representation. More specifically, the purpose of the present article is threefold:

- to quantify the relative importance of radiation, planetary boundary layer and cumulus subgrid scale processes to determine evaporation and precipitation in WRF simulations over the Mediterranean;

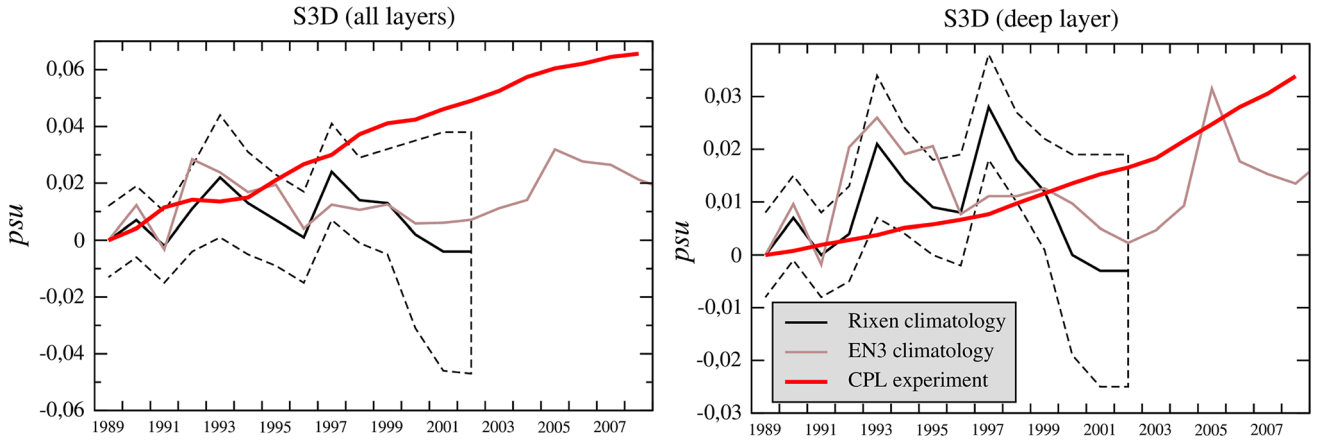

Fig. 1 Yearly mean time-series of the salt content averaged over the whole Mediterranean Sea (*left*) and over a deep layer below 600 m-depth (*right*). In *thick red*, for the period 1989–2008 from the WRF3.1-NEMO coupled simulation described in Drobinski et al. (2012). In *slight red*, for the period 1989–2009 from the EN3 (Ingleby and Huddleston 2007) estimations. In *black*, for the period 1989–2002 from the Rixen (2005) estimations, with the ±1 standard deviation interval in dashed lines

- to decompose the evaporation field according to the influence of forcing fields (e.g., surface exchange coefficients, moisture vertical gradients, wind speeds) in both observations and simulations as a means to determine the sources of evaporation biases;
- to select from the multi-physics ensemble those members that best simulate the MSWB in present conditions to used them for future forced/coupled simulations.

For the above purposes, version 3.3 of WRF (Skamarock et al. 2008) constitutes an outstanding tool because it can be run using a variety of state-of-the-art physical parameterizations. The MPE approach has been extensively used generally with the aim of selecting the set of parameterizations with the best performance over a given region and/or to simulate specific phenomena (Argüeso et al. 2011; Crétat et al. 2011; Evans et al. 2012; Flaounas et al. 2010; Jerez et al. 2013; Mooney et al. 2013; Ruiz et al. 2010). This study is of particular relevance in the context of the HyMeX (Hydrological cycle in the Mediterranean experiment; Drobinski et al. 2009; Drobinski et al. 2014) and MED-CORDEX (Mediterranean contribution to the Coordinated Regional climate Downscaling Experiment; Giorgi et al. 2009) programs for which the understanding and simulation of the MSWB constitute a major research topic.

The paper is structured as follows. The next section describes the RCM, the numerical experimental setup and the variance decomposition analysis used to separate the influence of each scheme. Section 3 gives a brief description of the datasets used to evaluate modelled results. Section 4 shows results of the sensitivity of the water budget to changes in the various parameterizations while Sect. 5 presents an evaluation of the model performance dependence on the choice of its physical setup by focusing on the sources of biases. Lastly, discussion and concluding remarks are given in Sect. 6.

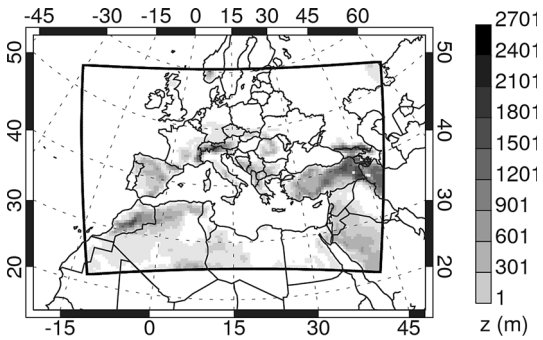

Fig. 2 Computational domain and the topography field as represented in the 50-km WRF simulations

2 Multi-physics ensemble and variance analysis

2.1 WRF RCM description and experimental setup

The multi-physics ensemble was constructed using version 3.3 of the WRF model using the Advance Research WRF (ARW) dynamic solver. WRF solves the compressible, non-hydrostatic Euler equations using a terrain-following vertical coordinate. In this study, the governing equations were discretized using a 50-km horizontal grid spacing and 28 sigma levels in the vertical with the top of the atmosphere set at 50 hPa. The domain of integration follows from the one suggested by the HyMeX and the MED-CORDEX experiments and contains a total of 116 by 78 grid points (in longitude and latitude respectively) and covers the entire Mediterranean Sea together with some

Table 2 Acronyms of the several radiation, planetary-boundary/surface layer and cumulus parameterizations schemes used to generate the multi-physics ensemble

Shortwave/longwave scheme (no)	PBL/SL scheme (no)	CU scheme (no)
Dudhia/RRTM (1)	YSU/MM5 similarity (1)	KF (1)
RRTMG/RRTMG (4)	MYJ/Eta similarity (2)	BMJ (2)
Goddard/Goddard (5)	MYNN/MM5 similarity (5)	SAS (4)
	ACM2/PX (7)	G3D (5)
		MT (6)
		NSAS (14)

The number associated with each parameterization in the WRF environment is denoted in parentheses

parts of Southern Europe, Northern Africa and a part of the Atlantic Ocean (see Fig. 2).

The MPE is then generated by performing a series of 1-year long numerical experiments combining four surface/planetary boundary layer (SPBL) schemes, six cumulus (CU) schemes and three atmospheric radiation (RAD) schemes. The simulated period starts on August 1 1994 and ends on July 31 1995 and, in the rest of the article, this period is designated as the year 1994–1995 for simplification.

Table 2 presents the acronym and the number associated with each parameterization in the WRF environment for the three schemes used to generate the ensemble. A brief description of each parameterization is given in the following subsections. All combinations are performed except for the combinations GR3D-YSU-RRTMG and GR3D-YSU-Goddard thus leading to a MPE containing a total of 70 members. Specifically, CU and SPBL schemes are expected to strongly influence the precipitation field whereas RAD and SPBL schemes are supposed to have a critical effect on the evaporation field. Although other components of the model can play an important role in the determination of the atmospheric water budget (e.g., microphysics scheme by changing precipitation amounts and cloudiness), the available ensemble of simulations allow us to explore a large range of responses. All simulations are performed using the same parameterizations of cloud microphysical and land surface processes and these correspond to the WRF Single moment 5-class (Hong et al. 2004) scheme and the Rapid Update Cycle model, respectively.

Sea surface temperatures together with initial and lateral boundary conditions were taken from the European Centre for Medium-Range Weather Forecast ERA Interim reanalysis (Dee et al. 2011). Lateral boundary conditions are provided every 6 h with a 0.75° horizontal grid spacing while SSTs are available on a $0.5° \times 0.5°$ latitude–longitude grid. The indiscriminate nudging technique (Salameh et al. 2010; Omrani et al. 2012b) is employed to drive the simulations over the interior domain in order to prevent a divergence of the WRF fields from the driving fields. The nudging is applied to all prognostic variables (zonal and meridional wind components, temperature and water vapor mixing ratio) in vertical levels above the planetary boundary layer (see Omrani et al. 2012a, b for details). The vegetation/land-use and elevation data come from the US Geological Survey 24-category dataset while soil type is based on a combination of the 10-min 17-category United Nations Food and Agriculture Organization soil data and US State Soil Geographic 10-min soil data.

2.2 Atmospheric radiation schemes

Short and long wave RAD schemes are used to determine the radiative cooling/heating rates at the ground surface and at any given atmospheric layer and determine to a large extent temperature lapse rates and the associated low levels instability. Three long wave schemes are considered in this study: the Rapid Radiative Transfer Model (RRTM, Mlawer et al. 1997), the RRTM for application to GCMs (RRTMG) and the Goddard (Shi et al. 2010) schemes. All three long-wave schemes interact with clouds, carbon dioxide, ozone and methane while only RRTMG and Goddard account for aerosols direct effect. Of the three short-wave options, Dudhia (1989) represents the least complex option accounting for clear sky scattering, water vapor aborption and cloud albedo and absorption. Goddard and RRTMG also include interactions with aerosols, ozone, carbon dioxide and other trace gases.

2.3 Surface and planetary boundary layer schemes

SPBL schemes are used in climate models to represent exchanges of momentum, moisture and heat between the surface and the atmosphere and their role to influence the evolution of the atmosphere mainly through turbulent vertical transports. Shin and Hong (2011) studied the sensitivity of various surface and near-surface variables to the choice of several planetary and surface layer schemes and showed that the variability of variables such as surface temperature and latent and sensible heat fluxes is mainly driven by the surface layer (SL) scheme rather than by the planetary boundary layer scheme no matter the stability regime. The importance of the planetary boundary layer (PBL) formulation can be however crucial in the precipitation field because it interacts with the cumulus scheme to determine the vertical distribution of heat and moisture. That is, it is expected that differences between SL scheme representations will dominate changes in the evaporation

field whereas differences across PBL schemes will dominate modifications in the precipitation field.

Over water, the evaporation is parameterized in the SL scheme using some bulk transfer formula (Stull 1988):

$$E = -\rho u_* q_* = \frac{\rho u_* k}{D(z_0, u_*, \psi(z/L))} \cdot dq_s = C_m \cdot dq_s, \qquad (2)$$

where ρ is the air density at the height z, u_* is the friction velocity, k the von Karman constant and $dq_s = q_s - q_l$ the difference between the saturation specific humidity at the surface (q_s; a function of SSTs) and the specific humidity at the lowest model level (q_l; in our case $z_l = 28$ m). The representation of surface exchange coefficients ($C_m = \rho u_* k / D(z_0, u_*, \psi(z/L))$) over water vary essentially due to the formulation of the function D through the roughness length (z_0) and the stability function ($\psi_m(z/L)$) where L is the Monin–Obukhov length scale. The Monin–Obukhov length scale ($L = -\overline{\theta_v} u_*^3 / kg\overline{w'\theta_v'}$) measures the stability of the surface layer and is generally positive for stable conditions and negative for unstable conditions. The surface layer instability can then be quantified by using the Monin–Obukhov stability parameter z/L with more stable (unstable) conditions as the value of z/L gets more positive (negative).

Four SPBL schemes are used to generate the MPE. The Yonsey University (YSU) PBL scheme described by Hong et al. (2006) is tied with the fifth-generation of the Mesoscale Model (MM5) SL scheme (Zhang and Anthes 1982) which is based on Monin–Obukhov similarity theory (Monin and Obukhov 1954). Over water, the Charnock relation $z_0 = \alpha_c \, u_*^2/g$ with $\alpha_c = 0.0185$ is used to relate the roughness length with the friction velocity (Charnock 1958).

Version 2 of the asymmetrical convective model (ACM2) PBL scheme (Pleim 2007) is tied with the Pleim-Xiu (PX) SL scheme (Pleim 2006). Over water, the roughness length in this SL scheme is computed as $z_0 = \alpha_c u_*^2/g + 1 \times 10^{-4}$ m with $\alpha_c = 0.032$.

The Mellor–Yamada–Janjic (MYJ) PBL scheme is described by Janjic (1990) and is based on the Mellor–Yamada closure model (Mellor and Yamada 1982). The MYJ PBL scheme is used with a SL scheme also based on Monin–Obukhov similarity theory (Monin and Obukhov 1954) with modifications introduced by Janjic (1994). Over water surfaces, a viscous sub-layer is explicitly parameterized following Janjic (1994) and near-surface conditions are then obtained from the interface between the viscous and the turbulent sublayers. The explicit treatment of a viscous layer may lead to important differences in the fluxes mainly when friction velocities are smaller than 0.7 m s^{-1}. The roughness length is given by the maximum between the Charnock approximation with $\alpha_c = 0.018$ and 0.0000159 m.

The Mellor–Yamada–Nakanishi–Niino (MYNN) PBL scheme (Nakanishi and Niino 2004) is also based on the Mellor–Yamada closure model (Mellor and Yamada 1982) but uses a different formulation of the mixing length. The MYNN scheme is tied with a modified version of MM5 SL scheme (Zhang and Anthes 1982) where the roughness length is calculated using the expression of Smith (1988) as $z_0 = \alpha_c u_*^2/g + 1.16 \times 10^{-5}/u_*$ with $\alpha_c = 0.016$.

2.4 Cumulus parameterization schemes

CU schemes represent the effects of subgrid scale processes on the formation of clouds and precipitation in climate models and also influence the vertical distribution of moisture and heat due to latent heat release and water vapor changes.

Six different CU schemes are used to generate the MPE. The Kain–Fritsch (KF) scheme used in WRF (Kain 2004) is the product of an update of its earlier parameterization (Kain and Fritsch 1990). The Betts–Miller–Janjic (BMJ) scheme is based on Betts (1993) with some modifications introduces by Janjic (1994). The Grell 3D ensemble (GR3D) scheme (Grell and Dévényi 2002) is based on the scheme of Grell (1993). The Modified Tiedtke (MT) scheme is based on the original Tiedtke scheme (Tiedtke 1989) with various modifications (Wang et al. 2004) that were briefly described by Zhang et al. (2011). The Simplified Arakawa-Schubert (SAS) scheme is a mass flux parameterization which is based on Arakawa and Schubert (1974) as simplified by Grell (1993). The new SAS (NSAS) scheme (Han and Pan 2011) is based on the SAS convection scheme.

2.5 Variance analysis

In this section, we present a method allowing to quantify the sensitivity of a given climate statistics to changes in the various parameterizations. Let us denote by X_{rpc} a given climate statistics (e.g., annual mean evaporation) derived from the simulation using the RAD scheme r ($\in [0, 2]$), the SPBL scheme p ($\in [0, 3]$) and the CU scheme c ($\in [0, 5]$) respectively. In each grid point, a MPE anomaly matrix can be defined by computing the difference between X_{rpc} and the value of X for the control run (X_{CTL}):

$$\Delta \mathbf{X} = \Delta \mathbf{X}_{rpc} = \mathbf{X}_{rpc} - X_{CTL}, \qquad (3)$$

where $\Delta \mathbf{X} = \Delta \mathbf{X}_{rpc} \in \Re^{70}$ and the CTL simulation is performed using RRTMG, YSU and KF schemes to parameterized RAD, SPBL and CU processes respectively. The CTL simulation uses the same physical package as version 3.1 WRF simulations that were shown to largely overestimate evaporation over the Meditaerranean (see Table 1).

A measure of the sensitivity of X to changes in the parameterizations can then be obtained by computing the variance of the anomaly matrix $\Delta\mathbf{X}$ as follows:

$$V = \sigma^2(\Delta\mathbf{X}) = \frac{1}{70}\sum_{rpc}(\Delta X_{rpc} - \overline{\Delta X_{rpc}})^2. \quad (4)$$

with $\overline{\Delta X_{rpc}}$ the mean anomaly across all members of the ensemble. In order to gain more insight on the contribution of each parameterization scheme to the total variability of the anomaly matrix, a variance decomposition method is used. The analysis follows directly from Déqué et al. (2007) with some minor modifications. Using an asterisk to represent the average with respect to the index it is substituted for, one can decompose the total matrix $\Delta\mathbf{X}_{rpc}$ as follows:

$$\begin{aligned}\Delta\mathbf{X}_{rpc} = {} & \Delta\mathbf{X}_{***} + (\Delta\mathbf{X}_{r**} - \Delta\mathbf{X}_{***}) + (\Delta\mathbf{X}_{*p*} - \Delta\mathbf{X}_{***}) \\ & + (\Delta\mathbf{X}_{**c} - \Delta\mathbf{X}_{***}) \\ & + (\Delta\mathbf{X}_{*pc} - \Delta\mathbf{X}_{*p*} - \Delta\mathbf{X}_{**c} + \Delta\mathbf{X}_{***}) \\ & + (\Delta\mathbf{X}_{r*c} - \Delta\mathbf{X}_{r**} - \Delta\mathbf{X}_{**c} + \Delta\mathbf{X}_{***}) \\ & + (\Delta\mathbf{X}_{rp*} - \Delta\mathbf{X}_{r**} - \Delta\mathbf{X}_{*p*} + \Delta\mathbf{X}_{***}) \\ & + (\Delta\mathbf{X}_{rpc} - \Delta\mathbf{X}_{*pc} - \Delta\mathbf{X}_{rp*} - \Delta\mathbf{X}_{r*c} \\ & + \Delta\mathbf{X}_{r**} + \Delta\mathbf{X}_{*p*} + \Delta\mathbf{X}_{**c} - \Delta\mathbf{X}_{***}), \end{aligned} \quad (5)$$

By construction, the covariance of any two terms between parentheses is zero and so the variance of $\Delta\mathbf{X}_{rpc}$ is equal to the sum of individual variances of each parentheses term. Using the same notation as Déqué et al. (2007) the total variance can be expressed as:

$$V = \sigma^2(\Delta\mathbf{X}_{rpc}) = R + P + C + RP + RC + PC + RCP, \quad (6)$$

where

$$R = \sigma^2(\Delta\mathbf{X}_{r**}), \quad (7)$$

$$RP = \sigma^2((\Delta\mathbf{X}_{rp*} - \Delta\mathbf{X}_{r**} - \Delta\mathbf{X}_{*p*} + \Delta\mathbf{X}_{***}) \quad (8)$$

and so on for other terms. Single terms (i.e., R, P and C) represent the contribution to the total variance coming from differences between the average change of two schemes of a given parameterization. That is, the term R will be different from zero if the mean change induced independently by simulations performed using the RRTM, the RRTMG and/or the Goddard schemes are different. Second order terms of the form RP, PC and RC represent the contribution of the interaction between two given parameterizations to the total variability.

With the aim of quantifying the relative importance of each subgrid-scale physical process in the determination of the total variance V, the total contribution of, for example the radiation scheme, can be estimated as follows:

$$\widehat{R} = R + \frac{RC}{2} + \frac{RP}{2} + \frac{RPC}{3}, \quad (9)$$

where $\widehat{R}$ contains all contributions and does not distinguish between those coming from single or interaction terms. Defined in this way, the sum of the three total contributions is equal to the total variance (i.e., $V = \widehat{R} + \widehat{P} + \widehat{C}$).

2.6 Sampling uncertainty estimation

An important issue when comparing the value of a given climate statistic (e.g., annual-mean precipitation in a given grid point) derived from two members of an ensemble is how to decide whether both quantities are different. Generally, a zero threshold cannot be used to decide if both quantities are different because, due to the use of finite length time series and the chaotic behaviour of climate models, even two simulations performed using the same climate model will show some numerical differences if they only differ, for example, on the initial conditions. That is, statistics derived from climate simulations inherently contain some sampling uncertainty.

Ideally, the sampling uncertainty in RCM simulations can be quantified by performing an ensemble of simulations employing slightly different initial conditions and/or using boundary conditions derived by running the driving model using slightly different initial conditions. The use of an ensemble of 70 simulations would render such analysis extremely costly in terms of computational resources and so we use an alternative way to quantify the sampling uncertainty based on a Monte Carlo approach. In this case, a large number of "equally possible" climate statistics are derived by sampling randomly over full time series in individual grid points. For example, in order to estimate the sampling uncertainty related with annual-mean values $\overline{X}$, time averaged quantities are computed 200 times by sampling randomly with replacement over the daily 1-year long time series, thus obtaining a distribution for $\overline{X}$ that can be denote by $\overline{X}^i$. A maesure of the sampling uncertainty is then obtained as twice the standard deviation of the 200 sample distribution (i.e., $2 \cdot \sigma(X^i)$).

A similar method to estimate sampling uncertainty was used by Déqué et al. (2011) and Di Luca et al. (2012b). Déqué et al. (2011) used a Monte Carlo procedure and a 10 members sampling and found a very good agreement between the sampling uncertainty computed using various runs only differing on initial conditions and the Monte Carlo approximation for time-averaged precipitation. For time-averaged temperature, they found a good agreement in summer season but they found that the Monte Carlo approximation underestimates by nearly 30 % the "true" spread in winter.

Table 3 Available and calculated variables for WRF simulations, HOAPS3 and OAFlux satellite products and the ERAI reanalyses

	Available	Calculated
WRF	E, P, C_m, $\|u_{10}\|$	$dq_s = E/C_m$
HOAPS3	E, P, $dq_{s\text{-}10}$, $\|u_{10}\|$	$dq_s = f(dq_{s-10},\ z_0)$
		$C_m = E/dq_s$
ERAI	E, P, $\|u_{10}\|$, $RH_{z(p)}$, $T_{z(p)}$, SST, p_s	$dq_{s\text{-}z(p)} = f(RH_p,\ T_p,\ SST,\ p_s)$
		$dq_s = f(dq_{s-z(p)},\ z_0)$
		$C_m = E/dq_s$
OAFlux	E, P, $dq_{s\text{-}2}$, $\|u_{10}\|$	$dq_s = f(dq_{s-2},\ z_0)$
		$C_m = E/dq_s$

Please, see the text for explanation of abbreviations

3 Evaluation datasets

3.1 HOAPS3 product

Version 3 of the Hamburg Ocean Atmosphere Parameters and Fluxes from Satellite Data (HOAPS3; Andersson et al. 2010) dataset provides an estimation of evaporation and precipitation over the global oceans using satellite retrievals. HOAPS3 monthly mean values are available over a 0.5° by 0.5° grid mesh while twice daily composites are available over an horizontal grid with a 1° horizontal spacing. Daily values are then simply calculated by averaging twice daily estimations. HOAPS3 products are derived from measurements performed using the Special Sensor Microwave Imager (SSM/I) radiometers and include the derivation of several parameters such as wind speed at 10 m height ($|u_{10}|$), 10-m atmospheric humidity (q_{10}) and precipitation (Andersson et al. 2010, 2011). SSTs are obtained from the National Oceanographic Data Center/Rosenstiel School of Marine and Atmospheric Science (NODC/RSMAS) Pathfinder dataset and are used to estimate the saturation moisture at the surface (q_s). From the former observed quantities, evaporation is then calculated as:

$$E_{HOAPS3} = \rho C_r |u_{10}|(q_s - q_{10}) = \rho C_r |u_{10}| dq_{s-10}, \qquad (10)$$

where ρ is the moist air density (calculated using q_{10}, the estimated air temperature, and a pressure of 1,013.25 hPa) and C_r is the moisture transfer coefficient computed using the Coupled Ocean-Atmosphere Response Experiment (COARE) 2.6a bulk flux algorithm (Fairall et al. 1996, 2003).

From daily values of E and $dq_{s\text{-}10}$ it is possible to compute an equivalent surface exchange coefficient (C_m) that can be used to directly evaluate the performance of WRF to simulate the same quantity. First, the 10-m vertical humidity gradient of HOAPS3 must be extrapolated to WRF vertical lowest level (i.e., $z = 28$ m) and this is simply done by assuming neutral stability in the surface layer (see Table 3):

$$dq_s = dq_{s-10} \cdot \frac{ln(z/z_0)}{ln(10/z_0)}, \qquad (11)$$

where a mean roughness length equal to 1.52×10^{-4} m (Peixoto and Oort 1992) is used. HOAPS3 precipitation is also based on microwave retrievals from SSM/I and uses a neural network approach trained by precipitation values from the European Centre for Medium-Range Weather Forecast model.

3.2 ERA-interim reanalysis

ERA Interim (ERAI; Dee et al. 2011) constitutes an improve global atmospheric reanalysis provided by the European Centre for Medium-Range Weather Forecast. Compared with ERA-40 reanalysis (Uppala et al. 2005), ERAI uses a more sophisticated data assimilation scheme and assimilates a greater number of observations leading to an improved representation of the hydrological cycle and a better temporal consistency on a range of time-scales (Dee et al. 2011). ERAI fields are available globally every 6 h over a mesh with a 0.75° grid spacing and a total of 37 pressure levels (from 1,000 to 1 hPa), from the 1st January 1979 onwards. In addition of the evaporation, precipitation and 10-m wind speed fields, relative humidity ($RH_{z(p)}$) and temperatures ($T_{z(p)}$) at the lowest pressure level above the surface together with surface pressure and SST values are used to estimate vertical humidity gradients ($dq_{s\text{-}z(p)}$, see Table 3). Again, Eq. 11 is used to convert the ERAI gradient $dq_{s\text{-}z(p)}$ to an equivalent WRF gradient. Once the value of dq_s is obtained, surface exchange coefficients (C_m) are derived from both E and dq_s (see Table 3 for details).

3.3 OAFlux product

The Objectively Analyzed air–sea Fluxes (OAFlux; Jin and Weller 2008) products are constructed not from a single data source, but by objectively combining ship-based observation, satellite retrievals (SSM/I radiometers) and

results from three atmospheric reanalyses (ERA-40, NCEP-1 and NCEP-2). As for the HOAPS3 dataset, latent heat fluxes are derived from independent estimations of 10-m wind speed, 2-m humidity and air temperatures and SSTs using version 3.0 of the COARE bulk flux algorithm (Fairall et al. 2003). Daily fields of all variables are available from 1985 over a grid mesh with a 1.0° grid spacing that includes global ocean basins free of ice. WRF-equivalent surface exchange coefficients are derived from daily values of E and dq_s after the vertical humidity gradient is extrapolate from 2 to 28 m using Eq. 11 (see Table 3).

3.4 GPCP product

The Global Precipitation Climatology Project (GPCP; Adler and Huffman 2003) has been built by merging satellite and rain gauge data for the period 1979–2008 and is available over a grid mesh with a 2.5° grid spacing on a monthly basis. Precipitation in grid points near the coast contain information from rain gauges in land and according to Sanchez-Gomez et al. (2011) this should lead to a positive bias compared to only oceanic precipitation values.

4 MPE spread in reproducing the annual-mean MSWB

The relative importance of the various subgrid-scale processes on the MSWB is assessed in this section using the variance decomposition method as described in Sect. 2.5. Figure 3a shows the standard deviation of evaporation differences between the MPE and the CTL run (i.e., the MPE CTL-anomaly) in each grid point over the Mediterranean Sea (see Eq. 4). Evaporation differences across simulations show important spatial heterogeneity with standard deviation values varying between 50 and 250 mm yr^{-1} and a mean value of 117 mm yr^{-1}. This value is somewhat smaller than the 164 mm yr^{-1} found by Sanchez-Gomez et al. (2011) for a 12-member multi-model ensemble likely related with the absence of interior nudging in individual members and with the considerably longer simulations (40- vs 1-year) used in their analysis that allows the inclusion of interannual variability in their estimations. Minimum values are observed in the south-western part of the Mediterranean near the Maroccan-Algerian coast and close to the Atlantic border. Relative large values appear to the south of France, near Turkish coastal regions and more generally in the central-western Mediterranean. The low values observed in the western part of the Mediterranean, near the Gibraltar Straight, are maybe related with the fact that all simulations share the same lateral boundary conditions and the general west to east flow gives little freedom to individual members of the MPE to develop their own behaviour in this region. This seems to be supported by the study of Sanchez-Gomez et al. (2008) that, using an ensemble of 13 RCMs driven by the same lateral boundary conditions, shows that the ratio between the spread across RCMs and the mean natural variability (i.e., a measure of the internal variability) maximizes far from the boundaries and to the east of the domain. In particular, this ratio tends to be very small in the western part of the domain due to the important control exerted by the lateral boundary conditions resulting from the pronounced westerly flow.

Figure 3b shows the standard deviation of the evaporation CTL-anomaly normalized by the MPE annual mean evaporation. The normalized quantity shows values varying between 0.06 and 0.14 thus showing relatively little spatial heterogeneity and suggesting that evaporation variability is mostly proportional to its mean value. Assuming a normal distribution for the perturbations, results in Fig. 3b suggest that about 95 % (i.e., two standard deviations) of the perturbed simulations will induced changes of at most 30 % of the total mean evaporation. In most of the Mediterranean Sea, the mean and the standard deviation of evaporation across members of the MPE show maxima during winter months and minima during late spring and early summer months (not shown).

The standard deviation of the precipitation CTL-anomaly in each grid point over the Mediterranean Sea (Fig. 3c) shows values that vary between 20 and 220 mm yr^{-1} with minima in the north-western part of the Mediterranean and the eastern coast of Tunisia and maxima in the central and western parts of the Mediterranean Sea. Interestingly, the normalized version of the standard deviation of precipitation (Fig. 3d) shows that the spread between members is not proportional to the mean precipitation. The normalized pattern thus reveals a large spatial heterogeneity with values varying between 0.12 and 0.62. That is, in relative terms, the spread between the MPE members is larger in precipitation than in evaporation. Moreover, the variability induced by the parameterization choice shows a clear north-south gradient with larger values in the southern part of the Mediterranean. This gradient is mainly explained by the general decrease of precipitation to the south. Also, as for the evaporation variable, most precipitation falls during winter season as a consequence of the passage of synoptic perturbations.

Figure 3e shows the standard deviation of the water budget MPE CTL-anomaly matrix. The spatial pattern follows closely that of evaporation with values varying between 40 and 220 mm yr^{-1} although the standard deviation of the control anomaly $E - P$ matrix tends to be more homogeneous. In relative terms (Fig. 3f), the influence of the choice of physical parameterizations on the

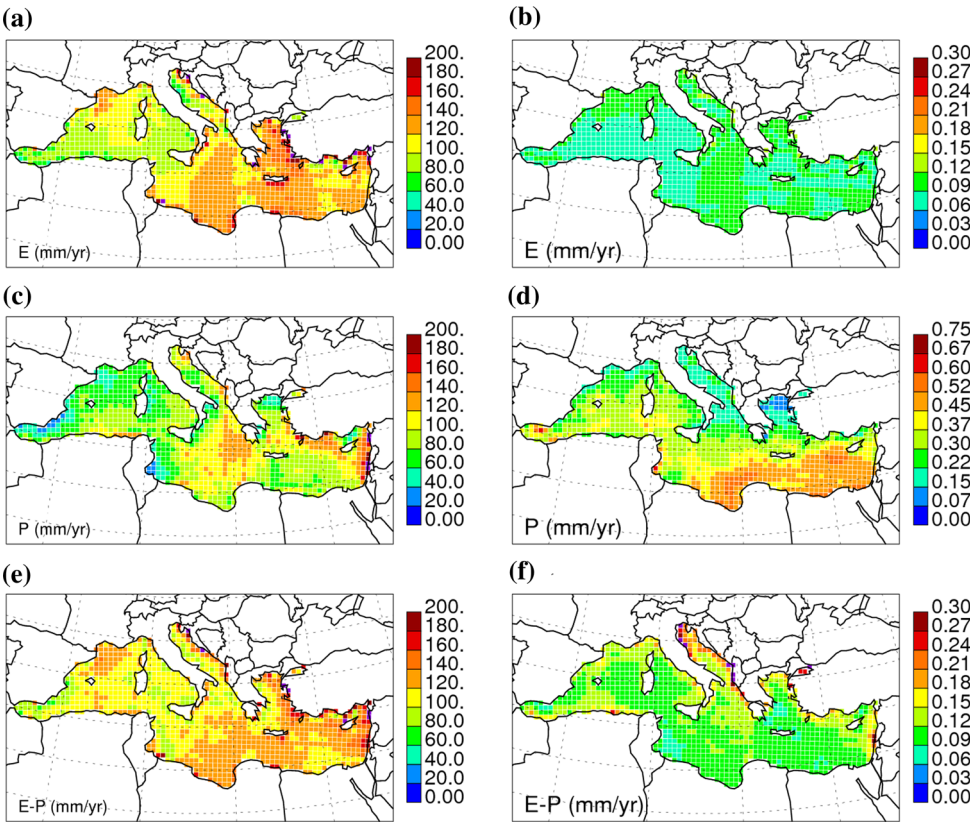

Fig. 3 Standard deviation of differences between members of the MPE and the CTL run (*left panels*) for simulated annual mean values of **a** evaporation (E), **c** precipitation (P) and **e** water budget (E–P). *Right panels* show the standard deviations normalized by the MPE annual mean values. **a** $\sqrt{V_{\mathrm{E}}}$. **b** $\sqrt{V_{\mathrm{E}}}/E_{mean}$. **c** $\sqrt{V_{\mathrm{P}}}$. **d** $\sqrt{V_{\mathrm{P}}}/P_{mean}$. **e** $\sqrt{V_{\mathrm{E-P}}}$. **f** $\sqrt{V_{\mathrm{E-P}}}/(E-P)_{mean}$

Table 4 Standard deviation of evaporation, precipitation and water budget and the percentage of explained variance by the various decomposition terms as described in Sect. 2.5

var	$\sqrt{V}(\frac{mm}{yr})$	R(%)	P(%)	C(%)	RP(%)	RC(%)	PC(%)	RPC(%)
E	119	5	58	2	3	1	15	14
P	95	9	25	48	2	3	5	8
E–P	121	1	28	36	2	4	12	16

All values correspond to the average over the whole Mediterranean Sea

water budget is generally smaller than 15 % of the MPE-mean with maxima close to 30 % in the northern part of the Adriatic Sea.

Table 4 shows areal-mean percentages of the total variance explained by each decomposition term (see Eq. 6) for the annual-mean evaporation, precipitation and water budget fields. Averaged over the Mediterranean, the variability of evaporation across the MPE is largely dominated by the choice of the SPBL scheme with little influence of the choice of the RAD and CU schemes. The variability of precipitation across simulations seems to be mostly determined by the choice of the CU scheme although with an important contribution of the choice of then the SPBL scheme and even some influence of the RAD scheme. The water budget is more or less equally sensitive to the choice of SPBL and CU schemes with almost no influence of the RAD scheme choice.

The variance decomposition approach shows that single terms tend to dominate total variances with their sum explaining 65, 86 % and 64 % for evaporation, precipitation and water budget respectively. The interaction between CU and SPBL schemes appears to explain some variability of the evaporation field with little influence on precipitation. No matter the field considered, terms related with the interaction between RAD and CU/SPBL schemes are very small.

Figure 4 shows spatial patterns of the total contribution terms $\widehat{R}$ (left panels), $\widehat{P}$ (middle panels), and $\widehat{C}$ (right panels) (see Eq. 9) for the evaporation (top panels), precipitation (center panels) and water budget (bottom panels), respectively. Various conclusions can be drawn from Fig. 4:

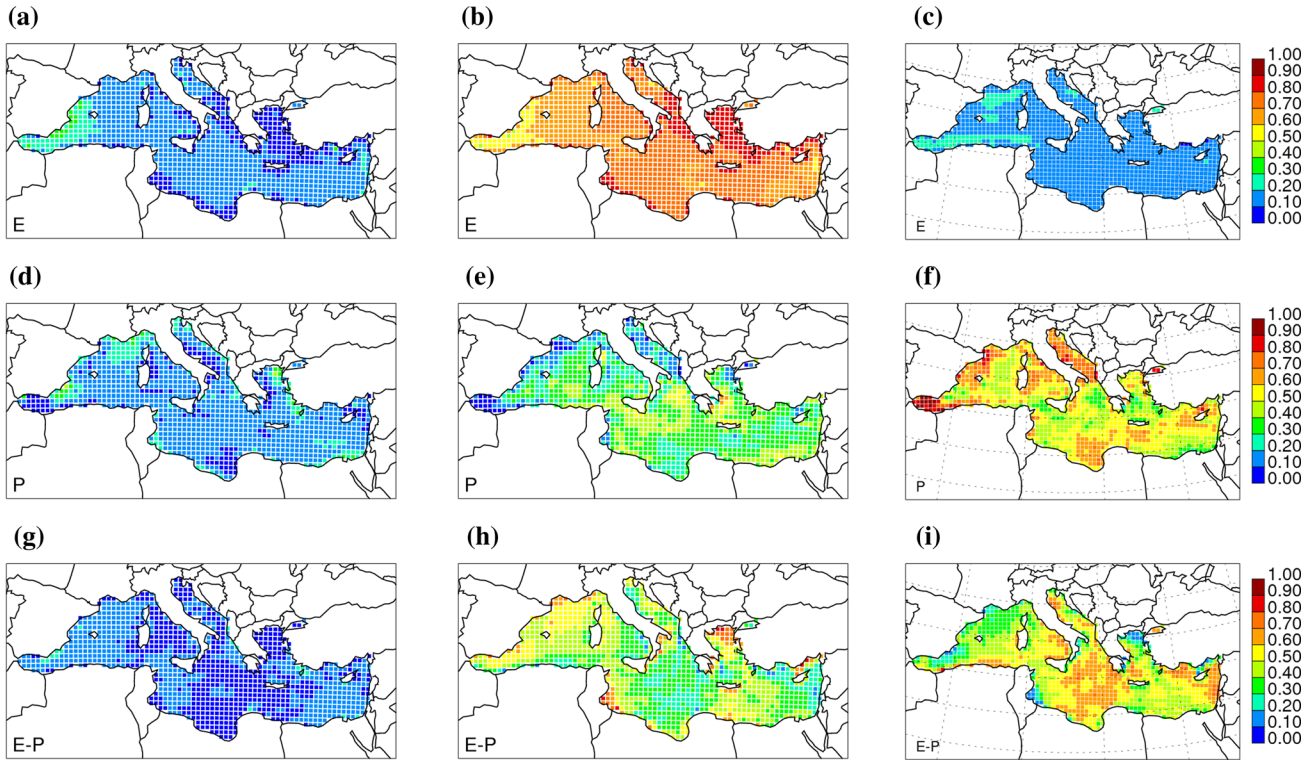

Fig. 4 Contributions from the RAD ($\widehat{R}$; *left pannels*), SPBL ($\widehat{P}$; *central pannels*) and CU ($\widehat{C}$; *right pannels*) schemes to the variance of the differences between the members of the MPE and the CTL member for annual means of evaporation (E; *top panels*), precipitation (P; *central panels*) and water budget (E–P; *bottom panels*). **a** $\widehat{R}_E$. **b** $\widehat{P}_E$. **c** $\widehat{C}_E$. **d** $\widehat{R}_P$. **e** $\widehat{P}_P$. **f** $\widehat{C}_P$. **g** $\widehat{R}_{E-P}$. **h** $\widehat{P}_{E-P}$. **i** $\widehat{C}_{E-P}$

- The influence of the choice of the RAD scheme is generally very small (smaller than 20 %) no matter the variable and the grid point considered.
- The choice of the SPBL scheme dominates evaporation variability across the MPE with relatively small spatial gradients.
- The proportion of the precipitation variability accounted by the CU and SPBL schemes depends strongly on the region considered. For example, the variability in the Adriatic Sea is mostly determined by the choice of the CU scheme while over the Ionian Sea the choice of the SPBL scheme seems to dominate.
- The variability of the water budget term is also determined by a near balance between SPBL and CU schemes.

That is, although mean evaporation values ($\approx$ 1,300 mm yr^{-1}) are much larger than mean precipitation values ($\approx$ 300 mm yr^{-1}), the greater variability across the MPE simulations for the precipitation variable implies that the choice of the SPBL and CU schemes is equally important in the determination of the water budget.

5 Performance of the MPE to simulate the annual-mean MSWB

Table 5 shows the 1994–1995 annual-mean evaporation, precipitation and water budget averaged over the Mediterranean Sea for the control run (WRF3.3-CTL), the MPE mean and two simulations performed using version 3.1 of WRF with the CTL physics package differing only on the initial conditions which are denoted by WRF3.1-CTL (a) and WRF3.1-CTL (b). Also shown are annual-mean values estimated using various observed and analyzed datasets. The comparison of the 1994–1995 annual mean values across the various datasets show qualitatively similar results to those obtained using 20-year periods (see Table 1):

- WRF3.1-CTL mean evaporation ($\approx$1,350 mm yr^{-1}) tends to overestimate observed mean values ($\approx$ 1,037$-$1,177 mm yr^{-1}) by about 20–30 %;
- WRF3.1-CTL mean precipitation ($\approx$ 320 mm yr^{-1}) is within the range of observed mean values ($\approx$ 237$-$468 mm yr^{-1}) although closer to the lower limit.
- WRF3.1-CTL mean water budget ($\approx$1,030 mm yr^{-1}) overestimates observed mean values by near 10–30 % ($\approx$ 606$-$940 mm yr^{-1}).

Table 5 1994–1995 annual mean values of evaporation (first column), precipitation (second column) and water budget (third column) as obtained from a variety of observed and simulated datasets (all in mm yr^{-1})

Data	*E*	*P*	*E* − *P*
WRF3.1-CTL (a)	1,348 (1,365)	318 (278)	1,030 (1,087)
WRF3.1-CTL (b)	1,355 (1,373)	328 (292)	1,027 (1,081)
WRF3.3-CTL	1,299 (1,319)	342 (300)	958 (1,019)
WRF3.3-MPE MEAN	1,286 (1,308)	281 (249)	1,005 (1,059)
ERA-40	1,037 (1,098)	382 (381)	655 (717)
ERAI	1,107 (1,187)	385 (345)	722 (742)
HOAPS3	– (1,177)	– (237)	– (940)
HOAPS3-GPCP	– (1,177)	468 (441)	– (736)
OAFlux-GPCP	1,120 (1,177)	468 (441)	606 (734)

All WRF simulations were performed using the CTL physics package, namely, RRTMG for the atmospheric radiation scheme, YSU for the surface/planetary boundary layer scheme and KF for the cumulus scheme. WRF3.1-CTL (a) and (b) simulations only differ on the initial conditions. Fields are averaged over the whole Mediterranean Sea and over the HOAPS3 domain for terms in parentheses

The simulation performed using the more recent 3.3 version with the CTL package (WRF3.3-CTL) also overestimates the annual-mean evaporation and water budget compared to observed values although showing a small improvement regarding the WRF3.1-CTL run. That is, although quantitative differences appear between simulations performed using the two versions of the WRF model, it is clear that the problem of the fresh water imbalance as reported in Sect. 1 remains in the newer WRF3.3 version, supporting the idea of using single 1994–1995 year simulations to study key factors leading to this imbalance.

5.1 Evaporation

Figure 5a presents the annual-mean field of evaporation in HOAPS3 showing that data is only available far from the coast over the open sea. Mean values vary from about 900 mm yr^{-1} in the western part of the domain to about 1,300 mm yr^{-1} in the eastern part mainly because of the spatial variations of the vertical humidity gradient term.

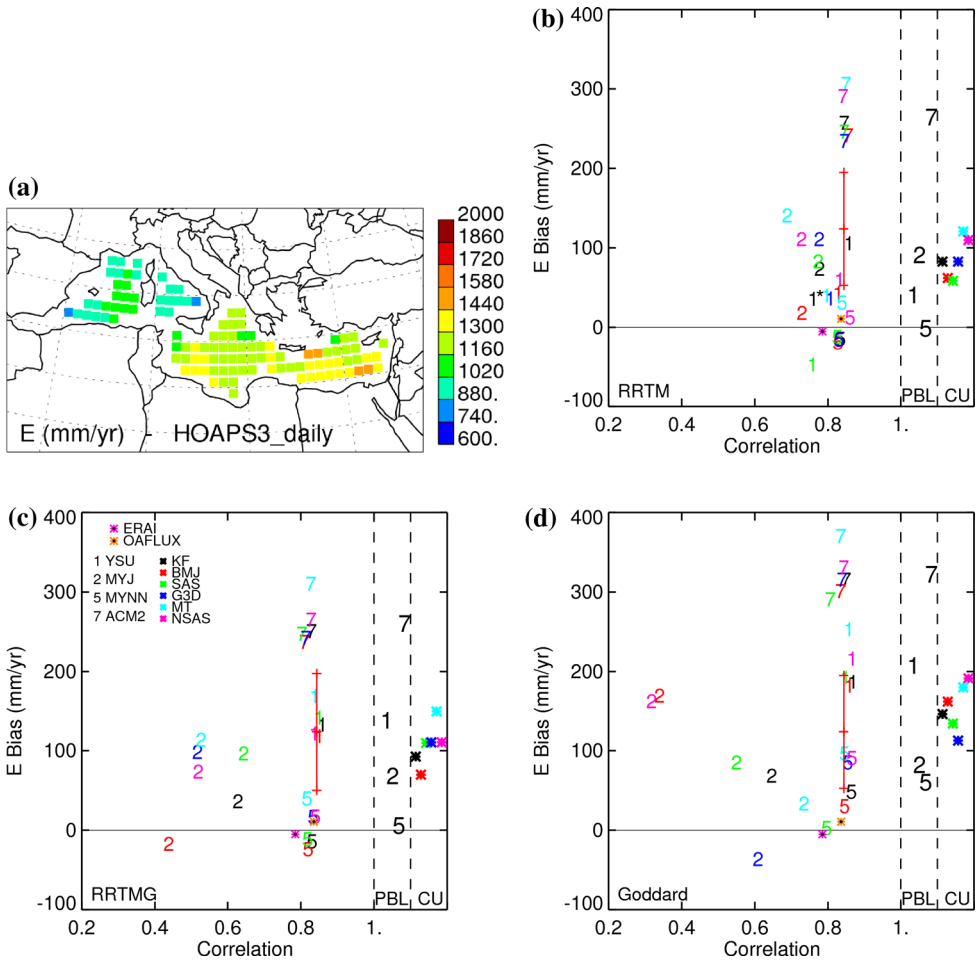

Fig. 5 **a** HOAPS3 annual-mean evaporation field and **b**–**d** biases in annual mean evaporation averaged over the Mediterranean Sea for the members of the MPE performed with the **b** RRTM, **c** RRTMG and **d** Goddard RAD subensembles as a function of spatial correlation compared to the HOAPS3 dataset. Mean biases across the various SPBL and CU subensembles are shown in the right side of each plot. The *red bar* gives an estimation of the sampling uncertainty associated with the CTL run (see Sect. 2.6 for details)

Figure 5b–d show annual mean differences compared to HOAPS3 for members of the MPE and the ERAI and OAFlux datasets as a function of their spatial correlations. For clarity reasons and considering that RAD schemes have relatively little influence in the evaporation field, results are shown separately for the RRTM (Fig. 5b), the RRTMG (Fig. 5c) and the Goddard (Fig. 5d) schemes. In all figures, numbers and colors indicate the SPBL and the CU schemes used to run each MPE member respectively. Biases are computed using data over the HOAPS3 domain and correlations are calculated using the nearest HOAPS3 grid point from either WRF simulations, ERAI reanalysis and OAFlux dataset. No matter the RAD scheme considered, members of the MPE show similar spatial patterns of annual-mean evaporation compared to HOAPS3 with mean spatial correlations that vary between 0.74 (RRTMG and Goddard) and 0.79 (RRTM). ERAI and OAFlux also show similar spatial distributions with correlation values of about 0.8 for both datasets. The only subensemble of simulations that tend to produce a different pattern compared to HOAPS3 are those performed using MYJ.

Averaged over the Mediterranean, ERAI and OAFlux mean biases are very small and always smaller than 15 mm yr^{-1} (i.e., $\leq$2 % of the mean evaporation) although it should be noted that such small values are partly explained by the compensation of positive and negative biases across the Mediterranean Sea (not shown). Mean biases between individual members and HOAPS3 span a great range of values varying from -30 to 400 mm yr^{-1} (i.e., 5–30 % of the mean evaporation) thus showing systematically larger values in simulations than in any observation-based dataset. According to the sampling uncertainty that characterize the CTL-run evaporation (red bar in Fig. 5b–d), significant differences between MPE members arise mostly when they are performed using a different SPBL scheme. That is, members of the ensemble using the same SPBL scheme (i.e., denoted with the same number) are clustered into groups showing similar $\overline{E}$ values. For example, simulations performed using the ACM2 PBL scheme (denoted with the number 7) systematically show higher evaporation than the CTL run that uses the YSU SPBL scheme (1). Similarly, runs using the MYNN SPBL scheme (5) tend to evaporate less than the CTL run, no matter the RAD scheme considered. Overall, simulations performed using the MYNN SPBL scheme show the best performances with annual mean biases of at most 100 mm yr^{-1} but generally within 50 mm yr^{-1} compared to HOAPS3 and ERAI/OAFlux.

In order to gain some insight on the causes of the general overestimation of evaporation in WRF simulations, the time-mean evaporation ($\overline{E}$) can be expressed as:

$$\overline{E} = \overline{C_m} \cdot \overline{dq_s} + cov(C_m, dq_s), \quad (12)$$

where $cov(C_m, dq_s)$ represents the temporal covariance between daily time series of C_m and dq_s. Figure 6 shows annual-mean values of C_m (Fig. 6a) and dq_s (Fig. 6b) together with the term $cov(C_m, dq_s)$ (Fig. 6c) for the HOAPS3 dataset. Averaged over the Mediterranean, $\overline{C_m}$ in HOAPS3 is 260 mm g $(yr\ kg)^{-1}$ with maximum values of about 300 mm g $(yr\ kg)^{-1}$ over the Gulf of Lion in southern France due to the high wind speeds ($\overline{|u_{10}|} \approx 7$ m s^{-1}) associated with Mistral and Tramontane wind systems in this region. Minimum values are found over the easternmost part of the Mediterranean Sea with values close to 200 mm g $(yr\ kg)^{-1}$ due to the relative low wind speeds in this region ($\overline{|u_{10}|} \approx 4.5$ m s^{-1}). The Mediterranean Sea-averaged $\overline{dq_s}$ in HOAPS3 is 4.4 g kg^{-1} and shows a west–east gradient with increasing values to the east of the Mediterranean mainly due to the spatial variation of SSTs and the related saturation specific humidity (q_s). The covariance between daily time series of C_m and dq_s is generally positive with values varying between -50 and 200 mm yr^{-1}. The covariance term explains near 4 % of the Mediterranean-averaged $\overline{E}$ and at most 20 % of $\overline{E}$ in any given grid point suggesting that time-mean evaporation is largely dominated by the product of time-mean quantities (i.e., $\overline{C_m} \cdot \overline{dq_s}$) with relatively little influence of the covariance term.

Figure 7 is the same as Fig. 5b–d but for $\overline{C_m}$ and $\overline{dq_s}$. Annual-mean surface exchange coefficients in ERAI and OAFlux are smaller than in HOAPS3 with Mediterranean Sea averaged values of 245 and 235 mm g $(yr\ kg)^{-1}$ respectively, leading to an observational uncertainty of about 10 % for Mediterranean averaged values. Although the spatial distribution of $\overline{C_m}$ in OAFlux is very similar to that of HOAPS3, ERAI shows a different pattern mainly due to the absence of the west-east gradient. Averaged over the HOAPS3 domain, annual-mean moisture vertical gradients are 4.7 and 4.8 g kg^{-1} in ERAI and OAFlux thus a bit larger than the HOAPS3. That is, although mean evaporation values are very similar in the three datasets, the way each dataset produces evaporation is somewhat different. Covariance terms for ERAI and OAFlux (not shown) are very close to the one in HOAPS3 with mean values of 27 and 65 mm yr^{-1} respectively and maxima over the Gulf of Lion.

$\overline{C_m}$ values as derived from WRF simulations show a great range of responses with annual mean values varying between 200 and 360 mm g $(yr\ kg)^{-1}$ depending essentially on the choice of the SPBL scheme and to a less extent on the RAD scheme. As for the evaporation field, differences across SPBL subensembles appear to be significantly larger than the sampling uncertainty which is about $\pm$12 mm g $(yr\ kg)^{-1}$. Compared with ERAI and OAFlux,

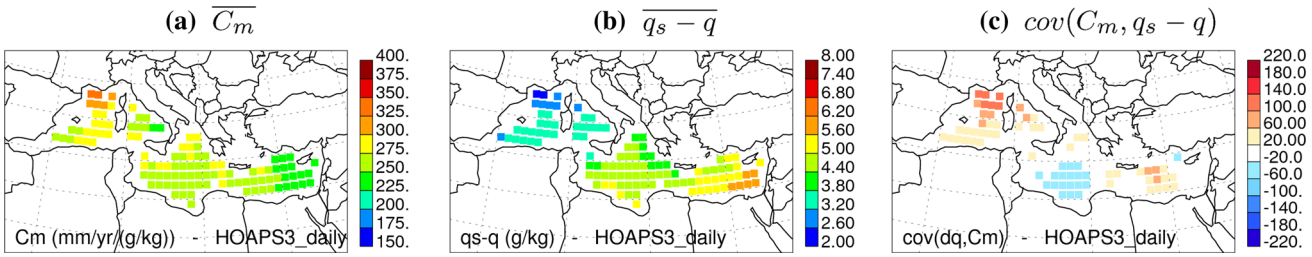

Fig. 6 HOAPS3 annual-mean values of **a** the surface exchange coefficient ($\overline{C_m}$), **b** the near-surface humidity gradient ($\overline{q_s - q}$) and **c** the temporal daily covariance of both quantities ($cov(C_m, dq_s)$). See Eq. 12 for details. **a** $\overline{C_m}$. **b** $\overline{q_s - q}$. **c** $cov(C_m, q_s - q)$

and to a less extent with HOAPS3, most simulations tend to overestimate surface exchange coefficients over the HOAPS3 domain except for members performed using the MYNN SPBL scheme that show relatively small biases compared to any observation dataset. Spatial patterns of $\overline{C_m}$ in individual members of the MPE generally agree well with the HOAPS3 pattern with correlations varying between 0.6 and 0.9.

For RRTMG and Goddard RAD schemes, annual-mean moisture vertical gradients in WRF simulations (Fig. 7d–f) tend to be slightly overestimated compared to HOAPS3 and show similar values as ERAI and OAFlux datasets. Moreover, RRTMG and Goddard simulations show little difference between them suggesting that the near surface humidity gradient is more or less insensitive to the SPBL/CU scheme choice. Much smaller values of $\overline{dq_s}$ are shown in simulations performed using the MYJ SPBL scheme thus somewhat compensating the relatively large values of $\overline{C_m}$ in that subensemble. Simulations performed using the RRTM scheme largely overestimate $\overline{dq_s}$ compared to any observed based dataset with a mean bias of 1.1 g kg^{-1}.

Results above show that the general overestimation of evaporation in WRF do not result from a single reason but rather depends on the particular simulation considered. In general, for simulations performed using the RRTM (RRTMG or Goddard) RAD scheme, the overestimation of $\overline{E}$ is mainly related with the large overestimation of the $\overline{dq_s}$ ($\overline{C_m}$) term. Specifically, simulations performed using the ACM2 SPBL scheme overestimate both $\overline{C_m}$ and $\overline{dq_s}$ and thus show the largest $\overline{E}$ values. For the YSU subensemble, the relative large values of $\overline{E}$ compared to HOAPS3 are related with an overestimation of either $\overline{dq_s}$ or $\overline{C_m}$ depending on the RAD scheme considered. The moderate overestimation of MYJ runs comes from larger values of $\overline{C_m}$ and a general good representation of $\overline{dq_s}$ values although showing a very high sensitivity to the choice of the CU scheme. Finally, MYNN SPBL members that showed the best performances to simulate evaporation also generally show the smallest biases in the simulation of both $\overline{C_m}$ and $\overline{dq_s}$ with bias values always within the observational uncertainty.

A further step in the evaluation of the performance of the WRF MPE to simulate the evaporation field can be made by comparing 10-m wind speeds with observations. Figure 8 shows the annual mean field of 10-m wind speed ($\overline{|u_{10}|}$) for HOAPS3 (Fig. 8a) together with Mediterranean Sea-averaged biases and spatial correlations for the MPE members, ERAI and OAFlux datasets (Fig. 8b). Only simulations performed using the RRTMG RAD scheme are shown but similar results are found for others RAD schemes. The spatial distribution of $\overline{|u_{10}|}$ in the MPE agrees quite well with the HOAPS3 pattern with spatial correlations ranging between 0.6 and 0.9. More interesting, ERAI and WRF simulations systematically show smaller values of Mediterranean Sea-averaged $\overline{|u_{10}|}$ compared to either OAFlux and HOAPS3 with differences of about 0.5 and 0.8 m s^{-1} respectively (i.e., about 10–15 % of $\overline{|u_{10}|}$). The underestimation of 10-m wind speed by both ERAI and WRF seems to be confirmed by comparing ERAI and 4 WRF simulation with HOAPS3 and QuikSCAT observations over the whole Mediterranean Sea for the period 2001–2005 (see Fig. 14a in Appendix 1). Also, the QuikSCAT satellite product was shown to outperform ERA-40 and NCEP reanalyses in reproducing 10-m wind speeds compared to in-situ measurements (buoy-mounted anemometers) over two sites in the Mediterranean Sea (Ruti et al. 2008).

The fact that differences between $\overline{|u_{10}|}$ across the MPE are mostly within the sampling uncertainty range ($\pm$0.2 m s^{-1}) and that WRF simulated wind speeds follows closely ERAI values suggest that WRF biases are at least partially explained by biases in the driving data. The observed underestimation in WRF simulations can have important consequences. Although surface coefficients C_m do not depend directly on $|u_{10}|$ but on the friction velocity u_* (see Eq. 2), a general increase (decrease) of $|u_{10}|$ will lead to an increase (decrease) of C_m values. As a consequence surface exchange coefficients in simulations would

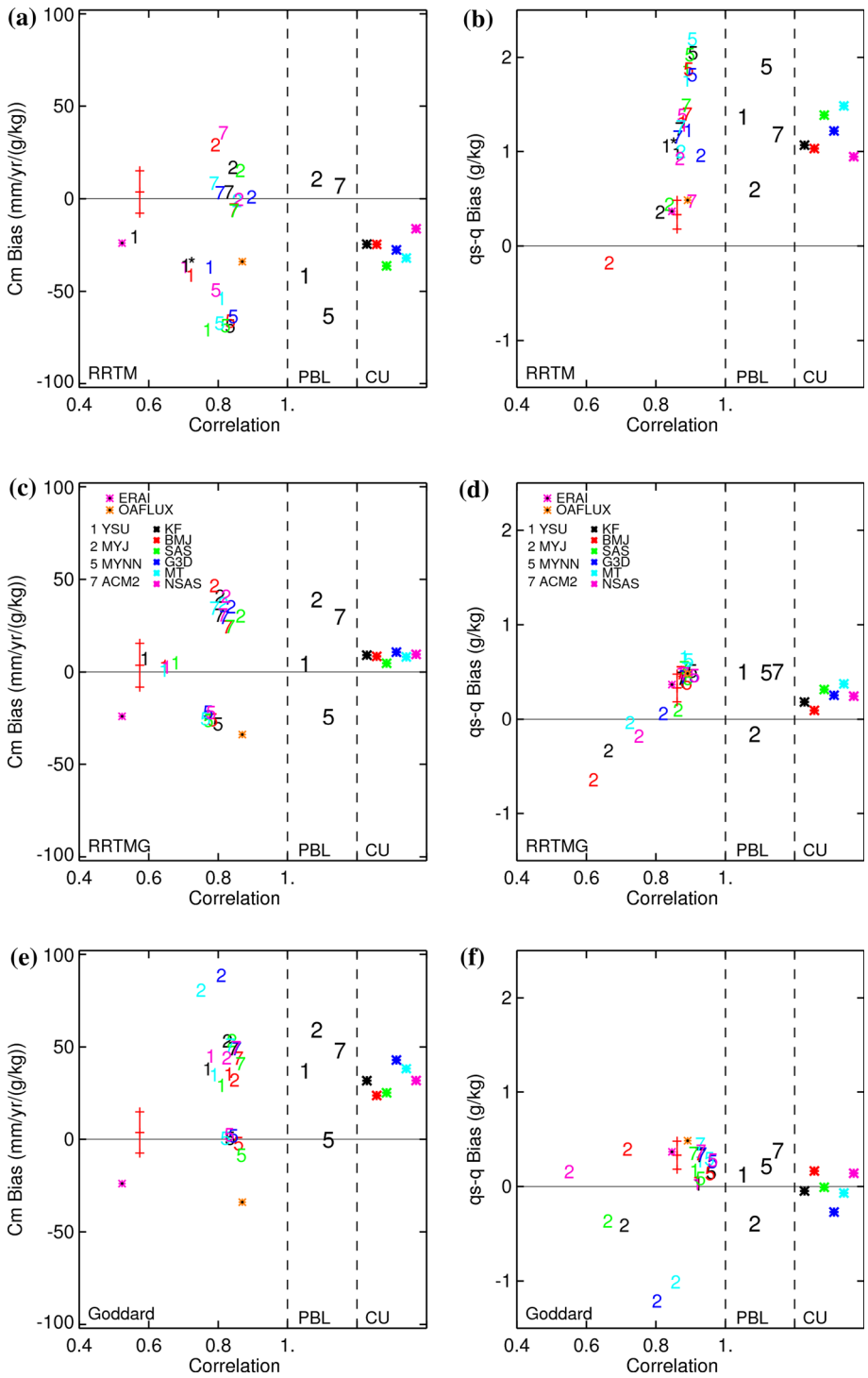

Fig. 7 Bias as a function of spatial correlations between the HOAPS3 fields and members of the MPE ensemble for the RRTM (*top panels*), the RRTMG (*central panels*) and the Goddard (*bottom panels*) RAD subensembles for the surface exchange coefficient (*left panels*) and the vertical humidity gradient (*right panels*). Mean biases across the various SPBL and CU subensembles are shown in the *right side* of each plot. The *red bar* gives an estimation of the sampling uncertainty associated with the CTL run (see Sect. 2.6 for details)

be larger if the driving data would give the right winds (e.g., HOAPS3 $|u_{10}|$ values). For example, the comparison between annual mean fields of $\overline{E}$ ($\overline{C_m}$) and $\overline{|u_{10}|}$ when pooling all grid points with similar moisture vertical gradients results in an increase of about 130 mm yr^{-1} in $\overline{E}$ (24 mm g (yr kg)$^{-1}$ in $\overline{C_m}$) for a 0.8 m s^{-1} anomaly in $\overline{|u_{10}|}$.

5.1.1 *Influence of SPBL schemes on evaporation*

As briefly discussed in Sect. 2.3, differences in the representation of evaporation across simulations appear due to differences in the friction velocity and/or the function $D = D(z_0, \psi(z/L))$ in the denominator. Figure 9a presents the annual mean field of friction velocity ($\overline{u_*}$) for the CTL run

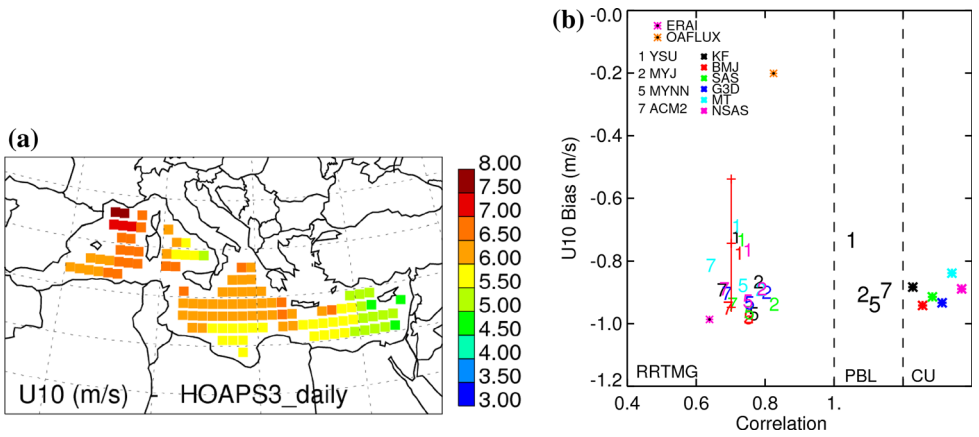

Fig. 8 **a** Annual-mean field of 10-m wind speed for the HOAPS3 dataset and **b** biases as a function of spatial correlations between individual members of the MPE and HOAPS3. ERAI and OAFlux bias and spatial correlations compared to HOAPS3 are also included. Only results from simulations performed using RRTMG RAD scheme are shown. Mean biases across the various SPBL and CU subensembles are shown in the *right side* of each plot. The *red bar* gives an estimation of the sampling uncertainty associated with the CTL run (see Sect. 2.6 for details)

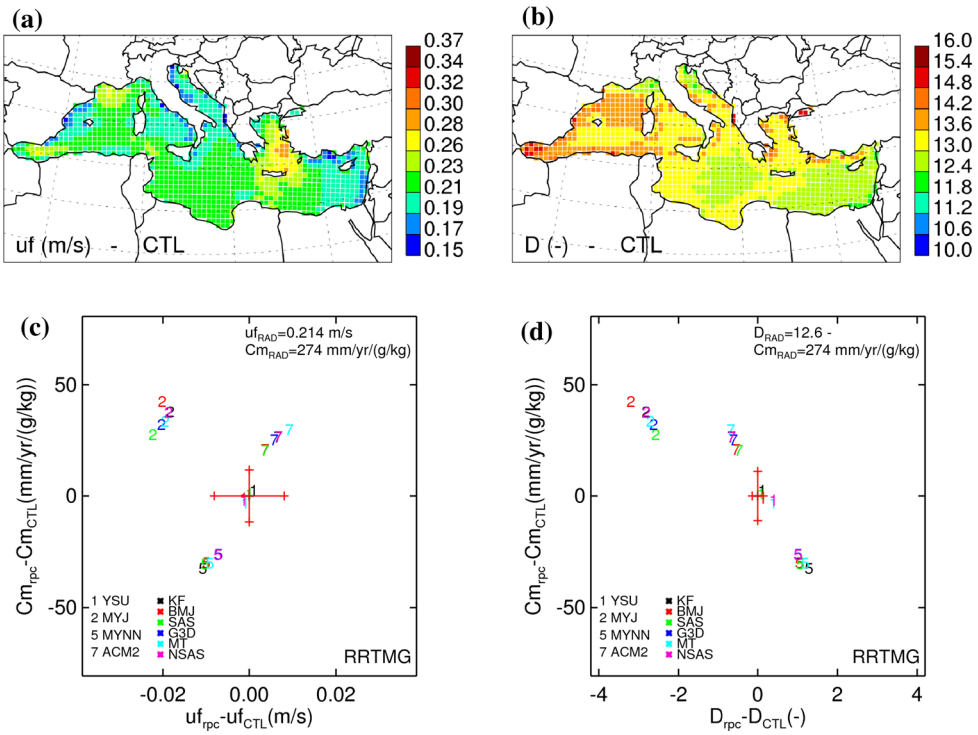

Fig. 9 CTL-run annual-mean fields of **a** the friction velocity and **b** the denominator function D (see Eq. 2). Mediterranean Seaaveraged differences between members of the MPE and the CTL member for the surface exchange coefficient as a function of differences in **c** the friction velocity and **d** the denominator function D. Only results from simulations performed using RRTMG RAD scheme are shown. *Red bars* give an estimation of the sampling uncertainty associated with the CTL run (see Sect. 2.6 for details)

showing that the spatial distribution of $\overline{u_*}$ follows closely the wind speed field. MPE simulations anomalies compared to the CTL run for $\overline{C_m}$ as a function of $\overline{u_*}$ are shown in Fig. 9c. For simplicity, only results obtained for simulations performed using the RRTMG RAD scheme are shown. Although $\overline{C_m}$ anomalies are always larger than the sampling uncertainty, $\overline{u_*}$ anomalies are generally within its sampling uncertainty range suggesting that changes in friction velocity do not determine surface exchange coefficient anomalies. Moreover, while $\overline{u_*}$ anomalies can partially explained the larger (smaller) values of $\overline{C_m}$ in the case of the ACM2 (MYNN) SPBL schemes, MYJ shows smaller $\overline{u_*}$ values with larger values of $\overline{C_m}$ suggesting that the relative large $\overline{C_m}$ values must come from changes in the denominator D.

The annual-mean field of D (Fig. 9b) shows larger values in the western part of the domain mainly due to more stable conditions in that region. Differences in $\overline{D}$ values between simulations and the CTL run (Fig. 9d) show that the choice of the SPBL scheme lead to

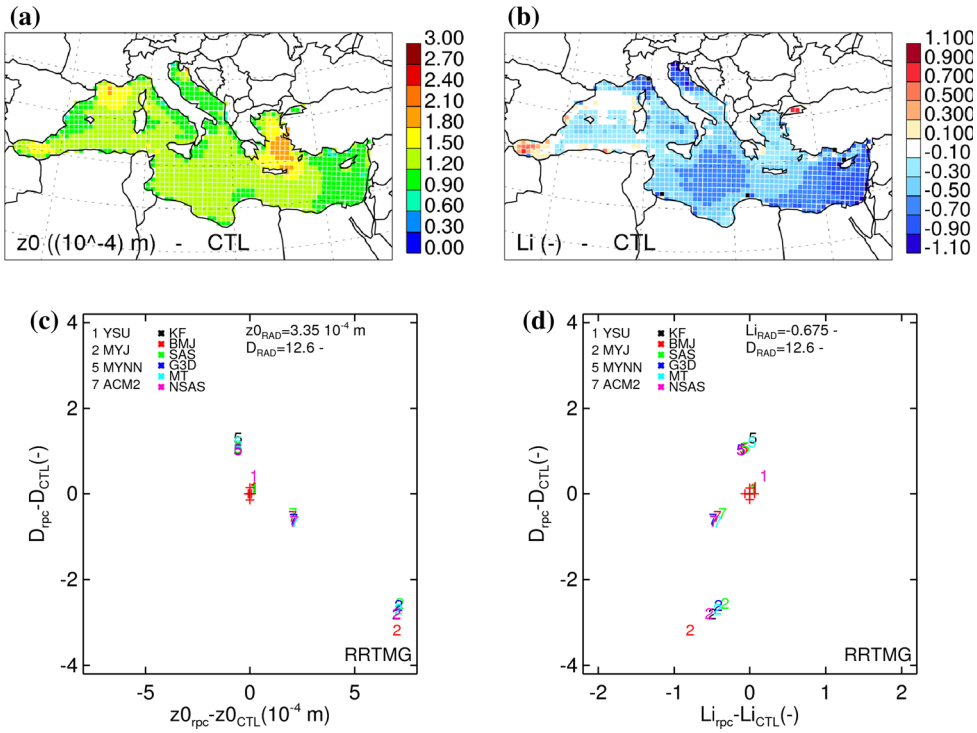

Fig. 10 CTL-run annual-mean fields of **a** the surface roughness (z_0) and the Monin–Obukhov stability parameter ($L_i = z/L$) (see Sect. 2.3 for details). Mediterranean Sea averaged differences between members of the MPE and the CTL run for the function D as a function of differences in **c** the surface roughness and **d** the Monin–Obukhov stability parameter. Only results from simulations performed using RRTMG RAD scheme are shown. *Red bars* give an estimation of the sampling uncertainty associated with the CTL run (see Sect. 2.6 for details)

significant differences (as large as 25 % of the $\overline{D}$) according to the sampling uncertainty measure. Smaller (larger) values of $\overline{C_m}$ are thus related with positive (negative) values of $\overline{D}$ anomalies in MYNN (MYJ and ACM2). As discussed in Sect. 2.3, changes in $\overline{D}$ can be accounted by either differences in the surface roughness (z_0) and/or in the Monin–Obukhov stability parameter ($L_i = z/L$). CTL-annual mean fields of $\overline{z_0}$ and $\overline{z/L}$ are shown in Fig. 10a, b respectively. Interestingly, the spatial pattern of $\overline{D}$ follows closely the pattern of $\overline{z/L}$ with maximum (minimum) values in the western (eastern) part of the Mediterranean. Anomalies of $\overline{D}$ as a function of $\overline{z_0}$ and $\overline{z/L}$ (Fig. 10c, d respectively) show that significant differences in $\overline{D}$ may arise due to differences in both parameters. For example, the relatively small values of $\overline{D}$ for MYJ members result from the combined effect of larger values of z_0 and smaller values of z/L (i.e., more unstable SL) although mainly due to changes in the former. The explicit formulation of the viscous layer in MYJ SL scheme tend to increase the effective z_0 compared to values obtained using the usual Charnock relation. Generally changes in $\overline{D}$ seems to be dominated by changes in the roughness length with the stability term playing a secondary role. Excepting MYJ, $\overline{z_0}$ differences across simulations are directly related with the magnitude of the Charnock constant (α_c) with the PX (MYNN) SL scheme showing the smallest (largest) values of $\overline{z_0}$ due to the largest (smallest) values of α_c.

5.1.2 *Influence of RAD schemes on evaporation*

As shown in Sect. 4, the influence of RAD schemes on the evaporation field is small compared with the influence of SPBL schemes. However, these small changes appear to be systematic and result from a compensation between changes in surface exchange coefficients and vertical humidity gradients.

Table 6 shows annual mean values of various quantities averaged over the Mediterranean Sea and over simulations performed using the same RAD scheme. Differences between evaporation values (first column in Table 6) across subensembles of simulations performed using the same RAD scheme span a range of about 60 mm yr^{-1} which is nearly 5 times smaller than the range span by SPBL subensembles. The range span by RAD subensembles when considering the Mediterranean averaged $\overline{C_m}$ ($\overline{dq_s}$) is of about 50 mm g $(yr\ kg)^{-1}$ (1.1 g kg^{-1}) that is similar (larger) than the same for SPBL subensembles. That is, RAD schemes have a primary influence on both $\overline{C_m}$ and $\overline{dq_s}$ but because large values of $\overline{C_m}$ are associated with small values of $\overline{dq_s}$, their total influence on evaporation is small.

Mean values of 2-m temperature (T_{2m}) are 293.4, 292.4 and 291.6 K for the RRTM, the RRTMG and the Goddard schemes respectively. Given that the mean SSTs are the same for all simulations ($\overline{SST} = 292.9$ K), differences in T_{2m} lead to different surface lapse rates and values of

Table 6 1994–1995 annual mean values of evaporation ($\overline{E}$), surface exchange coefficient ($\overline{C_m}$), moisture vertical gradient ($\overline{dq_s}$), 2-m temperature ($\overline{T_{2m}}$), sensible heat ($\overline{SH}$), Monin–Obukhov stability parameter ($\overline{z/L}$) and lowest-level specific humidity ($\overline{q_l}$)

Units	$\overline{E}$ (mm yr^{-1})	$\overline{C_m}$ (mm g (yr kg)$^{-1}$)	$\overline{dq_s}$ (g kg^{-1})	$\overline{T_{2m}}$(K)	$\overline{SH}$ (W m^{-2})	$\overline{z/L}$	$\overline{q_l}$ (g kg^{-1})
RRTM	1,262	242	5.5	293.4	1.1	0.32	9.0
RRTMG	1,274	274	4.6	292.4	9.3	−0.67	9.8
Goddard	1,320	295	4.4	291.6	16.7	−1.1	10.1

Columns shows values averaged across simulations performed using the same radiation scheme. All values are averaged over the whole Mediterranean Sea

sensible heat fluxes (*SH*) that are larger for smaller values of T_{2m}. As a result, the Goddard (RRTM) scheme subensemble shows the smallest (largest) values of the Monin–Obukhov stability parameter z/L and the largest (smallest) values of the surface exchange coefficient C_m due to the more unstable (stable) surface conditions. In turn, the larger values of C_m in Goddard explain the larger values in evaporation.

The effect on the stability term describe above tends to dominates evaporation variations across RAD subensembles and also have consequences on the vertical humidity gradient term. The larger values of evaporation lead to larger values of the specific humidity near the surface (q_l) that in turn appear to decrease vertical humidity gradients near the surface decreasing the initial differences in evaporation and partially offsetting the effect of RAD schemes on evaporation through changes in C_m.

5.2 Precipitation

The observational uncertainty in precipitation is quite large with annual-mean values of 237 mm yr^{-1} in HOAPS3, 345 (385) mm yr^{-1} in ERAI and 441 (468) mm yr^{-1} in the GPCP dataset when averaged over the HOAPS3 (whole Mediterranean Sea) domain (see Table 5). Precipitation totals in the HOAPS3 dataset are very small compared to ERAI and GPCP estimations mainly due to a deficit of precipitation in the southern and eastern part of the Mediterranean Sea (not shown). Romanou et al. (2010) argued that the relative small amounts of precipitation in HOAPS3 can be related with issues in the microwave retrievals that primarily detect precipitation that falls from cold ice clouds and may miss significant amounts of precipitation falling from warm, winter stratiform clouds. A comparison between total precipitation amounts in HOAPS3, ERAI and another independent satellite product (TRMM) over the period 2001–2005 (see Fig. 14b in Appendix 1) also confirms the HOAPS3 underestimation of precipitation. Taking advantage of the higher spatial resolution of ERAI compared to GPCP, in what follows we will consider that ERAI gives a more realistic representation of precipitation over the Mediterranean Sea.

Figure 11 shows the annual-mean precipitation field for ERAI (Fig. 11a) and the associated MPE member biases as a function of the spatial correlations (Fig. 11d). Only simulations performed using the RRTMG RAD scheme are shown because precipitation results depend little on the RAD scheme. It is seen that simulations performed with different CU and SPBL schemes show a large range of annual mean values. Biases compared to ERAI vary between −250 and 30 mm yr^{-1} showing that WRF simulations generally tend to produce too little precipitation. Spatial correlations between simulations and ERAI are very high with values varying between 0.8 and 0.9 suggesting that biases are likely to be related with a systematic underestimation everywhere over the Mediterranean Sea. In the right part of the plot, Fig. 11d also shows mean biases for subensembles of simulations using the same SPBL and CU schemes. Precipitation variability across the ensemble clearly results from the combined effect of both CU and SPBL schemes and some systematic changes are generally induced by individual schemes. For example, for any given CU scheme (i.e., any given colour), the order of SPBL schemes according to increasing values of precipitation (i.e., decreasing negative biases) gives always the same pattern: (1) MYJ (2), (2) MYNN (5), (3) YSU (1) and (4) ACM2 (7). Similarly, for a given SPBL scheme, the order of CU schemes according to increasing values of precipitation gives always the same pattern: (1) NSAS, (2) SAS, (3) KF, (4) G3D, (5) BMJ and (6) MT.

ERAI annual mean fields of convective and non-convective components of precipitation (Fig. 11b, c) show that approximately one fourth of the total precipitation (381 mm yr^{-1}) arises due to large-scale condensation (104 mm yr^{-1}) while the remaining precipitation (277 mm yr^{-1}) arises from the activation of the CU scheme. Convective precipitation anomalies in the MPE (Fig. 11e) are about 100 mm yr^{-1} and often significantly larger than the sampling uncertainty ($\approx \pm 60$ mm yr^{-1}). On the contrary, for the non-convective precipitation component (Fig. 11f), differences are generally smaller than 20 mm yr^{-1} and are generally not significant according to the sampling uncertainty ($\approx \pm 18$ mm yr^{-1}). Again, spatial patterns of precipitation in individual simulations are

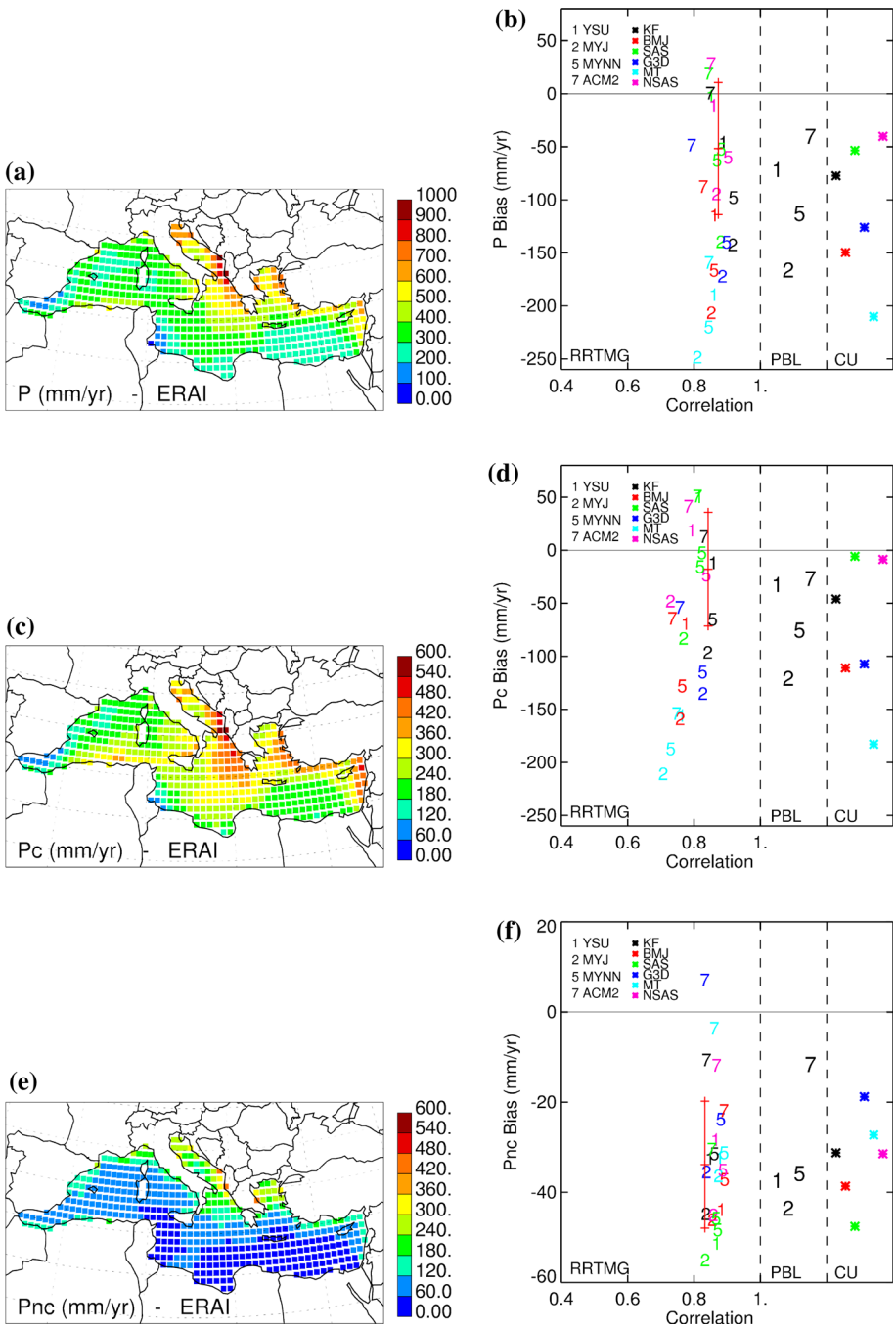

Fig. 11 ERAI annual-mean fields (*left panels*) and biases as a function of spatial correlations between ERAI and members of the RRTMG RAD multi-physics subensemble (*right panels*) for the total precipitation (*top panels*), the convective precipitation part (*middle panels*) and the non-convective precipitation part (*bottom panels*). Mean biases across the various SPBL and CU subensembles are shown in the *right side* of each plot. The *red bar* gives an estimation of the sampling uncertainty associated with the CTL run (see Sect. 2.6 for details)

similar to the ERAI pattern with spatial correlations showing values always larger than 0.75 with an overall average of 0.77 for the convective part and 0.83 for the non-convective part. Figure 11 shows that the simulated annual mean precipitation over the Mediterranean is underestimated compared to ERAI due to a deficit of both the convective and the non-convective terms. Because the convective part is proportionally larger than the non-convective part, total precipitation biases are dominated by biases in the convective term.

The factors controlling precipitation over the Mediterranean Sea are more difficult to determine than those controlling evaporation because there is no direct bulk formula describing precipitation amounts. Rather, precipitation results from various hypothesis about its triggering and duration. The difficulty is also enhanced because, as shown in Sect. 4, the causes leading to changes in precipitation requires to consider the behaviour of CU schemes together with those of SPBL schemes and probably their mutual interactions. In order to gain some insight

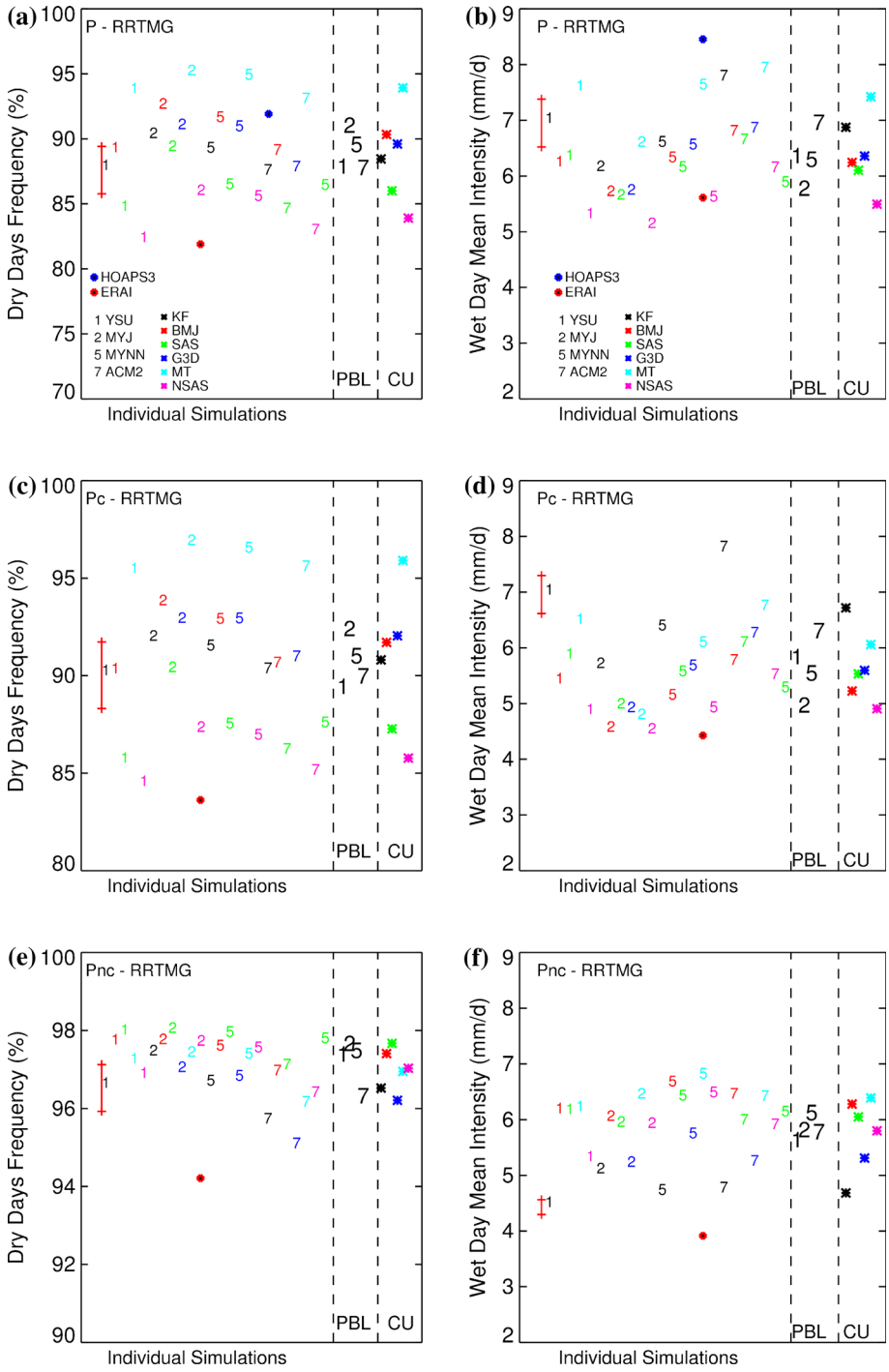

Fig. 12 Dry-day frequency (*left panels*) and wet-day mean precipitation intensity (*right panels*) for the total precipitation (*top panels*), the convective precipitation part (*central panels*) and the non-convective precipitation part (*bottom panels*). *Red* and *blue* asterix designate the ERAI and the HOAPS3 (when available) datasets and the combination of numbers and colors individual MPE members. SPBL and CU columns show subensemble averages across SPBL and CU schemes respectively. Only results from simulations performed using the RRTMG radiation scheme are shown

on the sources of these systematic differences, Fig. 12 shows the relative frequency of dry days (days with precipitation amounts smaller than 1.0 mm; top panels) and the mean precipitation intensity of wet days (i.e., non dry days; bottom panels) for ERAI, HOAPS3 (when available), individual members of the MPE and subensembles of simulations using the same SPBL and CU schemes. Dry days are computed from daily time series of precipitation in their original grids and then spatially averaged over the Mediterranean Sea thus retaining the information of precipitation distributions at their original resolution.

For total precipitation (Fig. 12a), the frequency of dry days in the ERAI reanalysis is 82 % and all simulations show a larger number of dry days with values varying between 82 and 95 %. Given that the ERAI horizontal grid spacing (near 75 km) is somewhat larger than that of WRF (50 km) it is expected to find a higher frequency of wet days in ERAI compared to WRF at least assuming a similar

performance (see for example Di Luca et al. (2012a)). However, differences between dry days in ERAI and MPE members cannot be explained solely by differences in the horizontal resolution and show to be dependent on the specific CU and SPBL scheme used by each member.

The comparison of mean total precipitation anomalies across CU subensembles (Fig. 11d) with dry day frequency and wet day mean intensities suggest that dry day frequency differences dominate changes in total amounts of precipitation. For example, simulations performed using the NSAS (MT) CU scheme that showed the largest (smallest) total precipitation amounts (349 vs. 179 mm yr^{-1}) also show the largest (smaller) number of wet days (16 vs. 6 %) with the minimum (maximum) mean intensity of daily events (5.5 vs. 7.5 mm/day). That is, differences in the number of wet days and the intensity of mean events somewhat compensate each other although the effect due to the number of raining days dominates. Assuming that the frequency of wet days can be used as a proxy of the frequency of the CU scheme activation (i.e., efficiency of the triggering), the above results suggest that the variability of precipitation across the MPE is mainly related with the way in which CU schemes represent the triggering more than the duration/intensity.

5.2.1 *Influence of SPBL and RAD schemes on precipitation*

The dependence of total precipitation amounts with the choice of the SPBL scheme is fundamentally different than the same for CU schemes. For example, simulations performed using the ACM2 (MYJ) SPBL scheme that showed the largest (smallest) total amounts of precipitation (344 vs. 224 mm yr^{-1}) also show the largest (smallest) mean precipitation on wet days (7.0 vs. 5.7 mm/day). Although both parameters (i.e., frequency and intensity) seem to explain total precipitation differences across SPBL schemes, more significant changes appear to be related with the mean intensity of wet days than with dry day frequencies. That is, differences between SPBL scheme formulations seem to induce more important changes in the duration/intensity (i.e., closure) of events that in their frequency (i.e., triggering).

An important variable that influences both frequency and intensity of precipitation events is the amount of water vapor available in the atmosphere. Mainly through differences in evaporation, the choice of the SPBL scheme induce significant changes in the available low-levels water vapor and consequently in total amounts of precipitation. Figure 13 shows CTL-run anomalies of the total precipitation as a function of low-levels integrated water vapor (q_{intll}) for the RRTMG RAD scheme subensemble. q_{intll} is computed as the mass-weighted vertical integral of specific humidity through the lowest 10 levels (i.e., under about 800 hPa). Figure 13 shows that for a given value of q_{intll} the

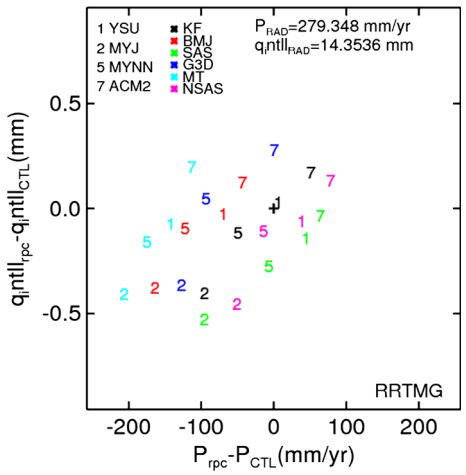

Fig. 13 Precipitation annual mean differences between members of the MPE and the CTL run as a function of differences of the low-levels integrated water vapor. Only results from simulations performed using the RRTMG RAD scheme are shown

amount of precipitation can change considerably for the various CU schemes suggesting that the efficiency to precipitate is strongly dependent on the choice of the CU scheme. Also interesting, for any given CU scheme (i.e., a given color), simulations tend to show increasing values of P as q_{intll} increases and the variation suggests an approximate linear relation. Although some values can show important discrepancies compared to this linear variation, the slope can be used to roughly quantify changes in $\overline{P}$ as a function of changes in $\overline{q_{intll}}$. Pooling all members of the MPE we obtain that, averaged over the Mediterranean Sea, precipitation increases by near 170 mm yr^{-1} for each kg/m^2 of water vapor added in low levels.

As stated before, differences in $\overline{q_{intll}}$ across SPBL schemes are generally related with differences in mean evaporation. For long-term mean values, the water budget is equal to the divergence of the horizontal water vapor flux ($\overline{E-P} = \overline{\nabla \cdot [q\mathbf{V}]}$) so a change in evaporation can lead to a change in precipitation and/or in the water vapor divergence. Table 7 shows that an excess of evaporation ($\Delta\overline{E} \geq 0$) between two SPBL subensembles generally leads to an increase of precipitation ($\Delta\overline{P} \geq 0$) together with larger amounts of the exported water ($\Delta(\overline{\nabla \cdot [q\mathbf{V}]}) \geq 0$) and larger values of the mean (equilibrium) integrated water vapor ($\Delta\overline{q_{intll}} \geq 0$). This partition is however dependent on the SPBL scheme. Simulations performed using the ACM2 (MYNN) SPBL scheme showing the highest (lowest) evaporation rate also show the largest values of $\overline{q_{intll}}$ and water vapor divergence ($\overline{\nabla \cdot [q\mathbf{V}]}$). While the MYNN subensemble shows the smallest values of $\overline{E}$ and $\overline{\nabla \cdot [q\mathbf{V}]}$, the smallest values of $\overline{q_{intll}}$ and $\overline{P}$ appear in simulations performed using the MYJ SPBL scheme suggesting that, in

Table 7 1994–1995 annual mean values of evaporation ($\overline{E}$), total precipitation ($\overline{P}$), water-vapor divergence ($\overline{\nabla \cdot [q\mathbf{V}]}$) and the integrated specific humidity ($\overline{q_{int}}$) for SPBL and RAD subensembles

Units	$\overline{E}$ (mm yr^{-1})	$\overline{P}$ (mm yr^{-1})	$\overline{\nabla \cdot [q\mathbf{V}]}$ (mm yr^{-1})	$\overline{q_{int}}$ (kg/m^2)
MYNN	1,175	254	921	14.3
MYJ	1,234	224	1,010	14.0
YSU	1,294	302	992	14.3
ACM2	1,438	344	1,094	14.6
RRTM	1,262	250	1,012	14.1
RRTMG	1,274	280	994	14.2
Goddard	1,320	313	1,007	14.5

All values are averaged over the whole Mediterranean Sea

relative terms, the export of water vapor tend to be larger in MYJ than in MYNN simulations.

The choice of the RAD scheme influences precipitation also through changes in the vertically integrated specific humidity. Table 7 shows that total precipitation mean values for individual RAD subensembles increase as the integrated low-levels water vapor increases. As shown in Sect. 5.1.2, increases in low level humidity are generally tied with evaporation increases. An important difference between SPBL and RAD schemes influence on precipitation is that precipitation differences across RAD subensembles are mostly related with changes in the non-convective part (not shown) as opposite to the response found across the various CU and SPBL schemes that tend to modify the convective part of precipitation. The mean non-convective precipitation values across simulations performed using the same radiation scheme are of 106, 71 and 53 mm yr^{-1} for the Goddard, the RRTMG and the RRTM schemes respectively.

6 Summary and discussion

Good quality simulations of the atmospheric component of the Mediterranean Sea water budget (i.e., mainly evaporation and precipitation) are of key importance to conduct atmosphere–ocean coupled RCM simulations in order to produce future climate projections. Recently, a particular configuration of the version 3.1 of the WRF RCM (Lebeaupin Brossier et al. 2011; Drobinski et al. 2012) was shown to overestimate the Mediterranean Sea water budget (defined as the difference between evaporation and precipitation) mainly due to an excess of evaporation thus compromising its use to perform coupled experiments. In this article we use a 70-member multi-physics ensemble to try to elucidate the relative importance and the role of various atmospheric subgrid scale processes in evaporation and precipitation. The physics ensemble was constructed by peforming 70 1-year long simulations using version 3.3 of the WRF regional climate model by combining 6 cumulus schemes, 4 surface/planetary boundary layer schemes and 3 radiation schemes.

The analysis concentrates on annual mean values with no explicit consideration of seasonal or daily variations of the various fields thus probably hiding errors that compensate when computing mean values. Moreover, a similar critique can be made for the spatial analysis that does not explicitly assess a number of climatically distinct basins over the Mediterranean Sea. Despite these limitations, a number of valuable conclusions can be drawn from the analysis.

First, a variance decomposition technique was used to separate the contribution of each parameterization scheme to the total variability of the evaporation, precipitation and water budget annual-mean fields across the multi-physics ensemble. Our results show that the spread in the evaporation field across the multi-physics ensemble is largely dominated by the choice of the surface/planetary boundary layer scheme that is shown to explain more than 70 % of the total variance. The precipitation variability across the multi-physics ensemble is determined by a balance between the choice of the cumulus (55 % of the total variance) and the surface/planetary boundary layer (32 % of the total variance) schemes with a strong regional dependence. Finally, although mean evaporation values ($\sim$1,300 mm yr1) are much larger than mean precipitation values ($\sim$300 mm yr1), the relative greater variability across simulations for the precipitation variable implies that the choice of the surface/planetary boundary layer (41 % of the total variance) and of the cumulus (50 % of the total variance) schemes are about equally important in the determination of the water budget.

The variance analysis also show that the spread obtained from a multi-physics ensemble can be nearly as large as the spread obtained from a multi-model ensemble (Sanchez-Gomez et al. 2011) depending on the variable being considered with precipitation showing relatively more dependence on the physics than the evaporation field. This last result is in agreement with Jerez et al. (2013) that using an 8-member physics ensemble found a similar spread compared to a multi-model ensemble for precipitation over the Iberian Peninsula.

Second, the influence of individual parameterization schemes on variables such as surface exchange coefficients, moisture vertical gradients, surface layer instability and low-levels water vapor was investigated to try to understand the sources of biases in evaporation and precipitation fields and to try to explain differences across members of the ensemble. Whenever possible, estimations from observations and reanalysis were included to ascertain about the performance of individual members of the

multi-physics ensemble. One reanalysis (ERA Interim) and different, although not independent, gridded observed datasets (HOAPS3 and OAFlux for evaporation; HOAPS3 and GPCP for precipitation) were used to evaluate the performance of simulations.

For evaporation our results suggest that:

- Averaged over the Mediterranean Sea, annual mean evaporation values as estimated from observations and reanalysis lead to a relatively small uncertainty not larger than 5 %. Uncertainties in surface exchange coefficients and near-surface moisture vertical gradients are larger with values near 10 %.
- Over the whole Mediterranean Sea, most members of the ensemble overestimate evaporation compared to observed datasets with biases varying between −30 and near 400 mm yr^{-1} depending on the member of the ensemble. This overestimation is generally related with an overestimation of surface exchange coefficients which are in turn related with too large values of the roughness length parameter and/or a surface layer which is too unstable. Roughness length values over sea are directly related with the value of the Charnock contant.
- The evaporation overestimation appears even though all simulations systematically underestimate 10-m wind speeds compared to observations by nearly 20 %. The negative wind speed biases are associated with similar biases in the driving fields. This result would imply an even larger overestimation of evaporation in the case that the WRF would be driven using the "right" boundary conditions.
- Although the influence of the choice of radiation schemes on evaporation is relatively small compared to the choice of the surface/planetary boundary layer scheme, radiation schemes strongly influence the variability of exchange coefficients and vertical humidity gradients near the surface. These influences are associated with changes in the surface layer stability due to modifications of temperature lapse rates.

For the precipitation variable, our results suggest that:

- The observational uncertainty of precipitation over the Mediterranean Sea is as large as precipitation mean values and prevent us to make any definite statement about the behaviour of the MPE members. ERAI reanalyses were considered as the best estimation due to the clear underestimation of the HOAPS3 dataset and the relatively low spatial resolution of the GPCP product.
- Most multi-physics ensemble members underestimate total precipitation amounts over the whole Mediterranean Sea compared with ERAI with biases varying between 20 and near −250 mm yr^{-1} mainly due to an overestimation of the number of dry days. The larger number of dry days in simulations is associated with deficits in the activation of cumulus schemes (i.e., efficiency of the triggering).
- Both radiation and surface/planetary boundary layer schemes influence precipitation through modifications of the available water vapor in the boundary layer that are tied with changes in evaporation.

In agreement with other studies (Argüeso et al. 2011; Evans et al. 2012; Fernández et al. 2007; Jerez et al. 2013; Mooney et al. 2013; Ruiz et al. 2010), we found that any of the members of the ensemble outperforms all the others for every variable and metrics although it is clear that some particular schemes perform very poorly. Our analysis show that simulations performed using either MM5/YSU or PX/ACM2 surface/planetary boundary layer schemes largely overestimate evaporation mean values while simulations performed using the Dudhia/RRTM radiation scheme show important biases in the simulation of moisture vertical gradients. Results also show that individual members using the MM5/MYNN surface/planetary boundary layer scheme generally outperform other members in the representation of the evaporation related variables (e.g., surface exchange coefficients, moisture vertical gradients, etc). Regarding the precipitation variable, the best performances are found for simulations using SAS and NSAS cumulus schemes with simulations using the KF cumulus scheme also showing good performances.

As already pointed out by other authors (Sanchez-Gomez et al. 2011), this study makes evident the need to improve our knowledge about the observed climatology over the Mediterranean Sea, mainly of the precipitation variable but also regarding other variables such 10-m wind speeds and surface humidity gradients that are useful to evaluate in more detail the representation of the evaporation in climate models. Finally, it should be noted that although this analysis is motivated by the use of atmosphere–ocean RCMs, the intensity and variability of air–sea fluxes will certainly differ in atmosphere–ocean coupled simulations. As a consequence, results and conclusions found in this study cannot be extrapolated to atmosphere–ocean coupled systems.

Acknowledgments The research reported here was supported by the École Polytechnique, by the French National Research Agency (ANR) project REMEMBER (contract ANR-12-SENV-001) and by the IPSL group for regional climate and environmental studies. EF was supported by the IMPACT2C program (funded by the European Union Seventh Framework Programme, FP7/2007–2013 under the grant agreement 282746). The authors are indebted to K. Beranger and T. Arsouze for their useful collaboration. The authors also thank K. Ramage, J. Lenseigne and all the Climserv team from IPSL for maintaining a user-friendly local computing facility and stored the various datasets used in this study. This work is a contribution to the HyMeX program through INSU-MISTRALS support and the MED-CORDEX. This research The authors wish to thank the project groups at the Hamburg Ocean Atmosphere Parameters and Fluxes from

Satellite Data Center, the European Centre for Medium-Range Weather Forecasts, the WHOI OAFlux project funded by the NOAA Climate Observations and Monitoring (COM) program and NASA Jet Propulsion Laboratory PO.DAAC for making their datasets readily available for this study.

Appendix 1: Support observations

See Fig. 14.

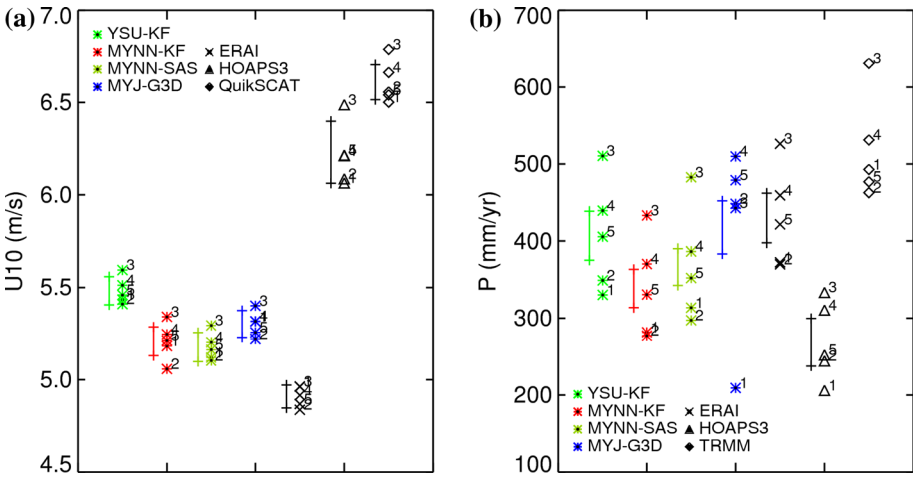

Fig. 14 Mediterranean Sea averaged values of annual mean fields of **a** 10-m wind speeds and **b** precipitation for a 5-year period between June 15th 2000 and May 31th 2005. For 10-m wind speed (precipitation) ERAI, HOAPS3 and QuikSCAT (TRMM) results are shown. All WRF simulations are performed using the RRTMG radiation scheme with the exception of simulation MYJ-G3D that was performed using the Goddard radiation scheme. Years are denoted by only one digit (i.e., 2001 is denoted by 1). The *error bar* in each case gives a measure of the internal varaibility as discussed in Sect. 2.6

References

Adler R, Huffman G (2003) The version-2 global precipitation climatology project (GPCP) monthly precipitation analysis (1979-present). J Hydrometeorol (4):1147–1167

Andersson A, Fennig K, Klepp C, Bakan S, Graß l H, Schulz J (2010) The Hamburg Ocean Atmosphere Parameters and Fluxes from Satellite Data HOAPS-3. Earth Syst Sci Data 2(2):215–234. doi:10.5194/essd-2-215-2010

Andersson A, Klepp C, Fennig K, Bakan S, Grassl H, Schulz J, Office M, Kingdom U, Wetterdienst D (2011) Evaluation of HOAPS-3 ocean surface freshwater flux components. J Appl Meteorol Climatol 50(2):379–398. doi:10.1175/2010JAMC2341.1

Arakawa A, Schubert WH (1974) Interaction of a cumulus cloud ensemble with the large-scale environment, Part I. J Atmos sci 31:674–701

Argüeso D, Hidalgo-Muñoz JM, Gámiz-Fortis SR, Esteban-Parra MJ, Dudhia J, Castro-Díez Y (2011) Evaluation of WRF parameterizations for climate studies over southern spain using a multistep regionalization. J Clim 24(21):5633–5651. doi:10.1175/JCLI-D-11-00073.1

Artale V, Calmanti S, Carillo A, DellAquila A, Herrmann M, Pisacane G, Ruti PM, Sannino G, Struglia MV, Giorgi F, Bi X, Pal JS, Rauscher S (2009) An atmosphereocean regional climate model for the Mediterranean area: assessment of a present climate simulation. Clim Dyn 35(5):721–740. doi:10.1007/s00382-009-0691-8

Béranger K, Drillet Y, Houssais MN, Testor P, Bourdallé-Badie R, Alhammoud B, Bozec A, Mortier L, Bouruet-Aubertot P, Crépon M (2010) Impact of the spatial distribution of the atmospheric forcing on water mass formation in the Mediterranean Sea. J Geophys Res 115(C12):C12,041. doi:10.1029/2009JC005648

Betts A (1993) The Betts-Miller scheme. The representation of cumulus convection in numerical models. Meteor Monogr 46:107–121

Charnock H (1958) A note on empirical wind-wave formulae. Q J R Meteorol Soc 84(362):443–447. doi:10.1002/qj.49708436212

Christensen J, Hewitson B, Busuioc A, Chen A, Gao X, Held I, Jones R, Kolli R, Kwon WT, Laprise R, Rueda V, Mearns L, Menendez C, Raisanen J, Rinke A, Sarr A, Whetton P (2007) Regional climate projections. Contribution of working group I to the fourth assessment report of the intergovernmental panel on climate change. In: Solomon S, Qin D, Manning M, Chen Z, Marquis M, Averyt K, Tignor M, Miller H (eds) Climate change 2007: the physical science basis, chap 11. University Press, Cambridge, pp 847–940

Crétat J, Pohl B, Richard Y, Drobinski P (2011) Uncertainties in simulating regional climate of Southern Africa: sensitivity to physical parameterizations using WRF. Clim Dyn 38(3–4):613–634. doi:10.1007/s00382-011-1055-8

Dee DP, Uppala SM, Simmons aJ, Berrisford P, Poli P, Kobayashi S, Andrae U, Balmaseda Ma, Balsamo G, Bauer P, Bechtold P, Beljaars aCM, van de Berg L, Bidlot J, Bormann N, Delsol C, Dragani R, Fuentes M, Geer aJ, Haimberger L, Healy SB, Hersbach H, Hólm EV, Isaksen L, Kå llberg P, Köhler M, Matricardi M, McNally aP, Monge-Sanz BM, Morcrette JJ, Park BK, Peubey C, de Rosnay P, Tavolato C, Thépaut JN, Vitart F (2011) The ERA-Interim reanalysis: configuration and performance of the data assimilation system. Q J R Meteorol Soc 137(656):553–597. doi:10.1002/qj.828

Déqué M, Rowell DP, Lüthi D, Giorgi F, Christensen JH, Rockel B, Jacob D, Kjellström E, Castro M, Hurk B (2007) An intercomparison of regional climate simulations for Europe: assessing uncertainties in model projections. Clim Change 81(S1):53–70. doi:10.1007/s10584-006-9228-x

Déqué M, Somot S, Sanchez-Gomez E, Goodess CM, Jacob D, Lenderink G, Christensen OB (2011) The spread amongst ENSEMBLES regional scenarios: regional climate models, driving general circulation models and interannual variability. Clim Dyn 38(5–6):951–964. doi:10.1007/s00382-011-1053-x

Di Luca A, de Elía R, Laprise R (2012a) Potential for added value in precipitation simulated by high-resolution nested regional climate models and observations. Clim Dyn 38(5–6):1229–1247. doi:10.1007/s00382-011-1068-3

Di Luca A, Elía R, Laprise R (2012b) Potential for added value in temperature simulated by high-resolution nested RCMs in present climate and in the climate change signal. Clim Dyn 40(1–2):443–464. doi:10.1007/s00382-012-1384-2

Drobinski P, Béranger K, Ducrocq V (2009) The HyMeX (Hydrological cycle in the Mediterranean Experiment) program: the specific context of oceanography. MERCATOR Quat Newslett:1–39

Drobinski P, Anav A, Lebeaupin Brossier C, Samson G, Stéfanon M, Bastin S, Baklouti M, Béranger K, Beuvier J, Bourdallé-Badie R, Coquart L, D'Andrea F, de Noblet-Ducoudré N, Diaz F, Dutay JC, Ethe C, Foujols MA, Khvorostyanov D, Madec G, Mancip M, Masson S, Menut L, Palmieri J, Polcher J, Turquety S, Valcke S, Viovy N (2012) Model of the regional coupled earth system (MORCE): application to process and climate studies in vulnerable regions. Environ Model Softw 35:1–18. doi:10.1016/j.envsoft.2012.01.017

Drobinski P, Ducrocq V, Alpert P, Anagnostou E, Béranger K, Borga M, Braud I, Chanzy A, Davolio S, Delrieu G, Estournel C, Filali Boubrahmi N, Font J, Grubisic V, Gualdi S, Homar V, Ivancan-Picek B, Kottmeier C, Kotroni V, Lagouvardos K, Lionello P, Llasat MC, Ludwig W, Lutoff C, Mariotti A, Richard E, Romero R, Rotunno R, Roussot O, Ruin I, Somot S, Taupier-Letage I, Tintore J, Uijlenhoet R, Wernli H (2014) HyMeX, a 10-year Multidisciplinary Program on the Mediterranean Water Cycle. Bull Amer Meteorol Soc. doi:10.1175/BAMS-D-12-00242.1

Dubois C, Somot S, Calmanti S, Carillo a, Déqué M, DellAquilla a, Elizalde a, Gualdi S, Jacob D, LHévéder B, Li L, Oddo P, Sannino G, Scoccimarro E, Sevault F (2011) Future projections of the surface heat and water budgets of the Mediterranean Sea in an ensemble of coupled atmosphereocean regional climate models. Clim Dyn 39(7–8):1859–1884. doi:10.1007/s00382-011-1261-4

Dudhia J (1989) Numerical study of convection observed during the winter monsoon experiment using a mesoscale two-dimensional model. J Atmos Sci 46(20):3077–3107

Evans JP, Ekström M, Ji F (2012) Evaluating the performance of a WRF physics ensemble over South-East Australia. Clim Dyn 39(6):1241–1258. doi:10.1007/s00382-011-1244-5

Fairall C, Bradley E, Rogers D (1996) Bulk parameterization of air–sea fluxes for tropical ocean-global atmosphere coupled-ocean atmosphere response experiment. J Geophys Res 101(C2):3747–3764

Fairall C, Bradley E, Hare J (2003) Bulk parameterization of air–sea fluxes: updates and verification for the COARE algorithm. J Clim 16:571–591

Fernández J, Montávez JP, Sáenz J, González-Rouco JF, Zorita E (2007) Sensitivity of the MM5 mesoscale model to physical parameterizations for regional climate studies: annual cycle. J Geophys Res 112(D4). doi:10.1029/2005JD006649

Flaounas E, Bastin S, Janicot S (2010) Regional climate modelling of the 2006 West African monsoon: sensitivity to convection and planetary boundary layer parameterisation using WRF. Clim Dyn 36(5–6):1083–1105. doi:10.1007/s00382-010-0785-3

Giorgi F, Christensen J, Hulme M, von Storch H, Whetton P, Jones R, Mearns L, Fu C, Arritt R, Bates B, Benestad R, Boer G, Buishand A, Castro M, Chen D, Cramer W, Crane R, Crossly J, Dehn M, Dethloff K, Dippner J, Emori S, Francisco R, Fyfe J, Gerstengarbe F, Gutowski W, Gyalistras D, Hanssen-Bauer I, Hantel M, Hassell D, Heimann D, Jack C, Jacobeit J, Kato H, Katz R, Kauker F, Knutson T, Lal M, Landsea C, Laprise R, Leung L, Lynch A, May W, McGregor J, Miller N, Murphy J, Ribalaygua J, Rinke A, Rummukainen M, Semazzi F, Walsh K, Werner P, Widmann M, Wilby R, Wild M, Xue Y (2001) Regional climate information-evaluation and projections. In: Houghton J (eds) Climate change 2001: the scientific basis. Contribution of working group I to the third assessment report of the intergovernmental panel on climate change. Cambridge University Press, Cambridge, pp 583–638

Giorgi F, Jones C, Asrar G (2009) Addressing climate information needs at the regional level: the CORDEX framework. Bull World Meteorol Org 58:175–183

Grell GA (1993) Prognostic evaluation of assumptions used by cumulus parameterizations. Mon Wea Rev 121:764–787

Grell GA, Dévényi D (2002) A generalized approach to parameterizing convection combining ensemble and data assimilation techniques. Geophys Res Lett 29(14):1693. doi:10.1029/2002GL015311

Guenard V, Drobinski P, Caccia JL, Campistron B, Benech B (2005) An observational study of the mesoscale mistral dynamics. Boundary-Layer Meteorol 115:263–288

Han J, Pan HL (2011) Revision of convection and vertical diffusion schemes in the NCEP global forecast system. Wea Forecast 26:520–533

Herrmann MJ, Somot S (2008) Relevance of ERA40 dynamical downscaling for modeling deep convection in the Mediterranean Sea. Geophys Res Lett 35(4):1–18. doi:10.1029/2007GL032442

Hong S, Dudhia J, Chen S, Korea S, Division MM (2004) A revised approach to ice microphysical processes for the bulk parameterization of clouds and precipitation. Mon Wea Rev 132:103–120

Hong SY, Noh Y, Dudhia J (2006) A new vertical diffusion package with an explicit treatment of entrainment processes. Mon Wea Rev 134:2318–2341

Ingleby B, Huddleston M (2007) Quality control of ocean temperature and salinity profiles–historical and real-time data. J Mar Syst 65:158–175

Janjic Z (1990) The step-mountain coordinate: physical package. Mon Wea Rev 118:1429–1443

Janjic ZI (1994) The step-mountain eta coordinate model: further developments of the convection, viscous sublayer, and turbulence closure schemes. Mon Wea Rev 122:927–945

Jerez S, Montavez JP, Jimenez-Guerrero P, Gomez-Navarro JJ, Lorente-Plazas R, Zorita E (2013) A multi-physics ensemble of present-day climate regional simulations over the Iberian Peninsula. Clim Dyn 40:3023–3046. doi:10.1007/s00382-012-1539-1

Jin X, Weller RAR (2008) Multidecade global flux datasets from the objectively analyzed air–sea fluxes (OAFlux) project: latent and sensible heat fluxes, ocean evaporation, and related surface meteorological variables. Technical Reports January, Woods Hole Oceanographic Institution, OAFlux Project Technical Report, Woods Hole. Massachusetts

Kain J, Fritsch J (1990) A one-dimensional entraining/detraining plume model and its application in convective parameterization. J Atmos Sci 47:2784–2802

Kain JS (2004) The Kain–Fritsch convective parameterization: an update. J Appl Meteorol 1980:170–181

Laprise R (2008) Regional climate modelling. J Comput Phys 227(7):3641–3666. doi:10.1016/j.jcp.2006.10.024

Lebeaupin Brossier C, Béranger K, Deltel C, Drobinski P (2011) The Mediterranean response to different spacetime resolution atmospheric forcings using perpetual mode sensitivity simulations. Ocean Model 36(1–2):1–25. doi:10.1016/j.ocemod.2010.10.008

Mariotti A, Struglia M, Zeng N, Lau K, Section C (2002) The hydrological cycle in the Mediterranean region and implications for the water budget of the Mediterranean Sea. J Clim 15(13):1674–1690

Mariotti A, Zeng N, Yoon JH, Artale V, Navarra A, Alpert P, Li LZX (2008) Mediterranean water cycle changes: transition to drier 21st century conditions in observations and CMIP3 simulations. Environ Res Lett 3(4):44,001. doi:10.1088/1748-9326/3/4/044001

Mellor GL, Yamada T (1982) Development of a turbulence closure model for geophysical fluid problems. Rev Geophys Space Phys 20:851–875

Mlawer E, Taubman SJ, Brown PD, Iacono MJ, Shepard A (1997) Radiative transfer for inhomogeneous atmospheres: RRTM, a validated correlated-k model for the longwave. J Geophys Res 102(D14):16,663. doi:10.1029/97JD00237

Monin AS, Obukhov AM (1954) Basic laws of turbulent mixing in the surface layer of the atmosphere. Trudy Geofiz Inst Acad Nauk SSSR 24(151):163–187

Mooney P, Mulligan F, Fealy R (2013) Evaluation of the sensitivity of the weather research and forecasting model to parameterization schemes for regional climates of europe over the period 1990–1995. J Clim 26:1002–1017. doi:10.1175/JCLI-D-11-00676.1

Nakanishi M, Niino H (2004) An improved MellorYamada level-3 model with condensation physics: its design and verification. Boundary-Layer Meteorol 112(1):1–31. doi:10.1023/B:BOUN.0000020164.04146.98

Omrani H, Drobinski P, Dubos T (2012a) Investigation of indiscriminate nudging and predictability in a nested quasi-geostrophic model. Q J R Meteorol Soc 138(662):158–169. doi:10.1002/qj.907

Omrani H, Drobinski P, Dubos T (2012b) Optimal nudging strategies in regional climate modelling: investigation in a Big-Brother experiment over the European and Mediterranean regions. Clim Dyn 138(668):1808–1813. doi:10.1007/s00382-012-1615-6

Peixoto J, Oort A (1992) Physics of climate. American Institute of Physics, New York

Peixoto JP, de Almeida M, Rosen R, Salstein D (1982) Atmospheric moisture transport and the water balance. Water Resourc Res 18(1):83–90

Pleim JE (2006) A simple, efficient solution of flux-profile relationships in the atmospheric surface layer. J Appl Meteorol Climatol 45(1):341–347

Pleim JE (2007) A combined local and nonlocal closure model for the atmospheric boundary layer. Part I: model description and testing. J Appl Meteorol Climatol 46(9):1383–1395. doi:10.1175/JAM2534.1

Rixen M (2005) The western Mediterranean deep water: a proxy for climate change. Geophys Res Lett 32(12):L12,608. doi:10.1029/2005GL022702

Romanou a, Tselioudis G, Zerefos CS, Clayson Ca, Curry Ja, Andersson a (2010) Evaporation precipitation variability over the Mediterranean and the Black Seas from satellite and reanalysis estimates. J Clim 23(19):5268–5287. doi:10.1175/2010JCLI3525.1

Ruiz JJ, Saulo C, Nogués-Paegle J (2010) WRF model sensitivity to choice of parameterization over South America: validation against surface variables. Mon Wea Rev 138(8):3342–3355. doi:10.1175/2010MWR3358.1

Ruti PM, Marullo S, D'Ortenzio F, Tremant M (2008) Comparison of analyzed and measured wind speeds in the perspective of oceanic simulations over the Mediterranean basin: Analyses, QuikSCAT and buoy data. J Mar Syst 70(1–2):33–48. doi:10.1016/j.jmarsys.2007.02.026

Salameh T, Drobinski P, Dubos T (2010) The effect of indiscriminate nudging time on large and small scales in regional climate modelling: application to the Mediterranean basin. Q J R Meteorol Soc 136(646):170–182. doi:10.1002/qj.518

Sanchez-Gomez E, Somot S, Déqué M (2008) Ability of an ensemble of regional climate models to reproduce weather regimes over Europe-Atlantic during the period 19612000. Clim Dyn 33(5):723–736. doi:10.1007/s00382-008-0502-7

Sanchez-Gomez E, Somot S, Josey Sa, Dubois C, Elguindi N, Déqué M (2011) Evaluation of Mediterranean Sea water and heat budgets simulated by an ensemble of high resolution regional climate models. Clim Dyn 37(9–10):2067–2086. doi:10.1007/s00382-011-1012-6

Shi J, Tao WK, Matsui T, Cifelli R, Hou A, Lang S, Tokey A, Wang NY, Peters-Lidard C, Jackson G, Rutledge S, Petersen W (2010) WRF simulations of the 20–22 January 2007 snow events over Eastern Canada: comparison with in-situ and satellite observations. J Appl Meteorol Climatol 49:2246–2266

Shin HH, Hong SY (2011) Intercomparison of planetary boundary-layer parametrizations in the WRF model for a single day from CASES-99. Boundary-Layer Meteorol 139(2):261–281. doi:10.1007/s10546-010-9583-z

Skamarock WC, Klemp JB, Dudhia J, Gill DO, Barker DM, Duda MG, Huang XY, Wang W, Powers JG, Mesoscale (2008) A description of the Advanced Res WRF Version 3. NCAR Technical Note, NCAR TN-475 June, p 113

Smith S (1988) Coefficients for sea surface wind stress, heat flux, and wind profiles as a function of wind speed and temperature. J Geophys Res 93(88):467–472

Somot S, Sevault F, Déqué M, Crépon M (2008) 21st century climate change scenario for the Mediterranean using a coupled atmosphereocean regional climate model. Global Planet Change 63(2–3):112–126. doi:10.1016/j.gloplacha.2007.10.003

Stull RB (1988) An introduction to boundary layer meteorology. Springer, Norman

Tiedtke M (1989) A comprehensive mass flux scheme for cumulus parameterization in large-scale models. Mon Wea Rev 117:1779–1800

Trigo IF, Bigg GR, Davies TD (2002) Climatology of cyclogenesis mechanisms in the Mediterranean. Mon Wea Rev 130(3):549–569

Uppala SM, Kllberg PW, Simmons AJ, Andrae U, Bechtold VDC, Fiorino M, Gibson JK, Haseler J, Hernandez A, Kelly Ga, Li X, Onogi K, Saarinen S, Sokka N, Allan RP, Andersson E, Arpe K, Balmaseda MA, Beljaars ACM, Berg LVD, Bidlot J, Bormann N, Caires S, Chevallier F, Dethof A, Dragosavac M, Fisher M, Fuentes M, Hagemann S, Hólm E, Hoskins BJ, Isaksen L, Janssen PAEM, Jenne R, Mcnally AP, Mahfouf JF, Morcrette JJ, Rayner NA, Saunders RW, Simon P, Sterl A, Trenberth KE,

Untch A, Vasiljevic D, Viterbo P, Woollen J (2005) The ERA-40 re-analysis. Q J R Meteorol Soc 131(612):2961–3012. doi:10.1256/qj.04.176

Wang Y, Leung LR, McGREGOR JL, Lee DK, Wang WC, Ding Y, Kimura F (2004) Regional climate modeling: progress, challenges, and prospects. J Meteorol Soc Jpn 82(6):1599–1628. doi:10.2151/jmsj.82.1599

Zhang C, Wang Y, Hamilton K (2011) Improved representation of boundary layer clouds over the southeast Pacific in ARW-WRF using a modified Tiedtke Cumulus parameterization scheme. Mon Wea Rev 139(11):3489–3513. doi:10.1175/MWR-D-10-05091.1

Zhang D, Anthes RA (1982) A high-resolution model of the planetary boundary layer-sensitivity tests and comparisons with SESAME-79 data. J Appl Meteorol 21(11):1594–1609